Surfaces and Interfaces 62 (2025) 106267

Contents lists available at ScienceDirect

Surfaces and Interfaces

journal homepage: www.sciencedirect.com/journal/surfaces-and-interfaces

Precision Laser Manufacturing and Metrology of Nature-Inspired Bioactive Surfaces for Antibacterial Medical Implants

Sara Hawi [a], Saurav Goel [b,c,*], Vinod Kumar [d,e], Claudiu Giusca [a], Oliver Pearce [f], Wayne Nishio Ayre [g]

[a] Surface Engineering and Precision Centre, Cranfield University, Cranfield MK43 0AL, UK
[b] London South Bank University, 103 Borough Road, London SE10 AA, UK
[c] University of Petroleum and Energy Studies, Dehradun 248007, India
[d] Magan Centre for Applied Mycology, Faculty of Engineering and Applied Sciences, Cranfield University, Cranfield MK43 0AL, UK
[e] Department of Bioscience and Bioengineering, Indian Institute of Technology Roorkee, Uttarakhand 247667, India
[f] Milton Keynes University Hospital, Milton Keynes MK6 5LD, UK
[g] Cardiff University, Cardiff CF14 4XY, UK

ARTICLE INFO

Keywords:
Laser ablation
Surface structuring
Bacterial adhesion
Fractal dimension
Orthopaedic implant

ABSTRACT

Femtosecond laser ablation presents a highly promising method to create bioactive nano/micro-structured metallic surfaces, offering numerous avenues for fabricating diverse types of surface structures. However, the relationship between surface properties and biological functionality, leading to the observed bioactivity remains unclear. This study aimed to investigate the relationship between structured/patterned steel surfaces and bioactivity, identifying key factors that enhance their performance. As opposed to the commonly used controversial parameter, arithmetic surface roughness (Ra), fractal dimension analysis was discovered to be strongly representative in quantifiably evaluating the adhesion of *Staphylococcus aureus* NCTC 7791 and MG-63 osteoblast-like cells. Surface chemistry and surface energy of structured surfaces showed no significant influence on bacterial adhesion. A specific type of laser-induced periodic structured surfaces with sub-micron wavelengths, high fractal dimension, and high texture aspect ratio demonstrated a 63 % reduction in bacterial adhesion compared to flat surfaces while avoiding cytotoxicity to MG-63 cells. Our findings underline the importance of scale-dependent analysis and the use of fractal analysis in evaluating the effectiveness of laser-structured surfaces for orthopaedic implant applications.

1. Introduction

Patterned and structured surfaces, now widely recognised as metasurfaces [1] are revolutionising cutting-edge technological applications across diverse sectors, including 5 G telecommunications [2], healthcare [3], cutting tools [4] and metrology [5].

In healthcare, these bioactive surfaces have transformative potential, especially in combating microbial infections through physical mechanisms that bypass the escalating crisis of antibiotic resistance [6]. This research study seeks to advance the current landscape of patterned biosurfaces by decoding the fundamental principles underlying surface structuring and its influence on bioactivity. Specifically, we investigate whether structured steel surfaces can selectively target bacterial cells while sparing bone cells, a critical distinction for developing effective bacterial eradication strategies. This knowledge is pivotal for designing surfaces that mitigate microbial contamination in high-traffic areas (e.g., train stations, airports, hospitals) without relying on chemically driven sanitization processes. Furthermore, such strategies could significantly benefit the orthopaedic sector by addressing the persistent challenge of surgical site infections (SSIs) during implant surgeries.

Abbreviations: AFM, Atomic force microscope; ANOVA, Analysis of variance; CA, Cell area; CC, Cell circularity; CFU, Colony forming units; CN, Cell number; DAPI, 4′,6-diamidino-2-phenylinode; ECM, Extracellular matrix; FE-SEM, Field emission scanning electron microscope; HSFL, High-spatial-frequency laser induced periodic structured surfaces; HSS, Hierarchically structured surfaces; LIPSS, Laser induced periodic surface structures; NCTC, National collection of type cultures; OD, Optical density; S. aureus, Staphylococcus aureus; SEM, Scanning electron microscope; SFE, Surface energy; Triton-X-100, 4-(1,1,3,3-Tetramethylbutyl)phenyl-polyethylene glycol; TSB, Tryptic soya broth; XDLVO, Extended Derjaguin, Landau, Verwey, Overbeek; XPS, X-ray photoelectron spectroscopy.

* Corresponding author.
E-mail address: goeLs@Lsbu.ac.uk (S. Goel).

https://doi.org/10.1016/j.surfin.2025.106267
Received 16 December 2024; Received in revised form 7 March 2025; Accepted 18 March 2025
Available online 20 March 2025

Recent data from 168 NHS hospitals in the UK in the year 2020–21 revealed that approximately 0.5 % of hip and knee replacement patients were readmitted due to SSIs [7], with studies indicating a 2.5 to 7-fold increase in mortality risk for patients developing deep infections [8]. Thus, structured surfaces that minimise bacterial retention offer a dual advantage: (i) reducing or eliminating the need for antibiotics, thereby curbing antibiotic resistance, and (ii) providing a sustainable, long-term solution to microbial contamination.

A critical question that remains unanswered is whether these micro/nano-structured surfaces inadvertently suppress bone cell adhesion, which could undermine their healthcare benefits. Addressing this question is essential for optimising surface designs that balance antibacterial efficacy with biocompatibility. Current literature highlights two primary approaches to creating bioactive surfaces, as illustrated in Fig. 1(a). Chemical methods, such as release-kill coatings, rely on the deposition of antimicrobial agents (e.g., copper, silver) that release ions to kill bacteria. However, these methods often suffer from issues such as delamination, debris release and uncontrolled burst release of active agents [9]. However, burst release rather than controlled release for both release-kill coatings and ion implantation remains a major issue.

In contrast, physical methods, such as adhesion prevention and contact-killing mechanisms, offer a more sustainable alternative by avoiding chemical resistance development. Recent advancements in ion implantation have emerged as a promising alternative to traditional coatings, addressing some of these limitations while still facing challenges related to controlled release.

Passive physical methods, inspired by natural self-cleaning surfaces like lotus leaves, shark skin, fish scales and butterfly wings, have evolved over millions of years to exhibit remarkable anti-adhesive and antimicrobial properties [10]. The "lotus effect," for instance, leverages hierarchical micro/nano-topography to create superhydrophobic surfaces that minimize wetting and adhesion [11]. Fig. 1(b) illustrates the nanostructures found on lotus leaves and butterfly wings, which are responsible for their exceptional self-cleaning capabilities [12]. Building on these natural paradigms, our study explores how engineered micro/nano-structured surfaces can replicate and enhance these properties for practical applications.

This research work is an effort to propel the domain of surface and interface science by providing novel insights into the interplay between surface topography, bioactivity and biocompatibility. By systematically investigating the selective interaction of structured surfaces with bacterial and bone cells, we aim to establish design principles for next-generation bioactive surfaces. These principles will not only improve the performance of antimicrobial surfaces but also expand their applicability across healthcare and other high-impact sectors.

To create micro- and nanostructured patterned surfaces, a variety of manufacturing techniques have been developed, each offering unique advantages and inherent limitations. These methods include nano-imprinting, photolithography, multi-tip diamond turning, hydrothermal treatments, micro-injection moulding, reactive ion etching, electron-beam lithography, and scanning probe lithography [13,14]. All methods have relevant bottlenecks in relation to the type of material, design complexity of geometry and multi-length scale hierarchical structure fabrication (micro and nanoscale) that they can produce. A critical analysis of the current manufacturing capability representing the achievable feature size with respect to the throughput is represented in Fig. 2. Among the various micro- and nano-fabrication methods, ultrashort pulsed laser ablation stands out as a powerful technique for creating multiscale structured surfaces over large areas on a wide range of materials.

Laser structuring has been shown to affect biological function (i.e. bacterial, bone cell and stromal cell function and differentiation). For instance, several studies have shown that rough surfaces can promote the entrapment of fibrin protein, adhesion of osteogenic cells, differentiation of stromal cells and boost the formation of a mineralised matrix [27]. Despite an initial success, a key question remains unaddressed in the literature, which is whether the topographical surface characteristics influence bacterial adhesion and osseointegration in a similar fashion or distinctly. Also, whether arithmetic mean surface “roughness” parameters such as average profile roughness (R_a) average areal roughness (S_a), root-mean-square (RMS) profile roughness (R_q), and RMS areal roughness S_q can reliably be used to infer bioactivity of the surface or whether a more robust indicator is required to more accurately described the bioactivity of a surface. It is also not known whether surface energy of

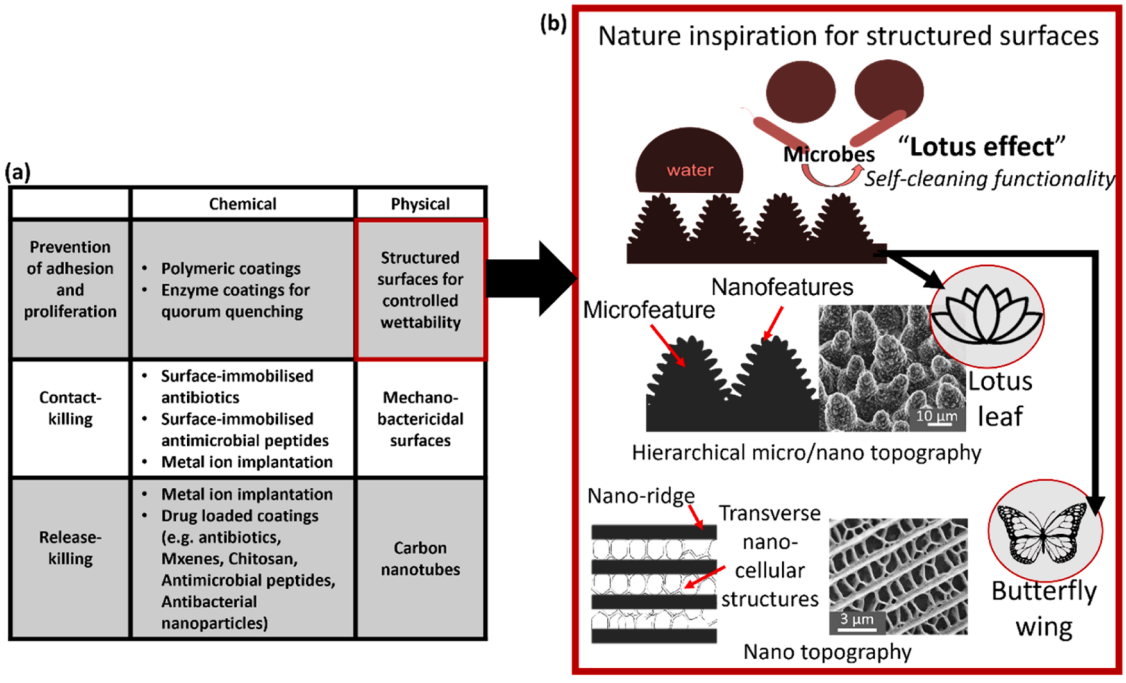

Fig. 1. (a) Different approaches and strategies of antibacterial surfaces. (b) Natural inspiration for antibacterial structured surfaces based on the lotus effect: structure of the lotus leaf and butterfly wing (Author’s contribution).

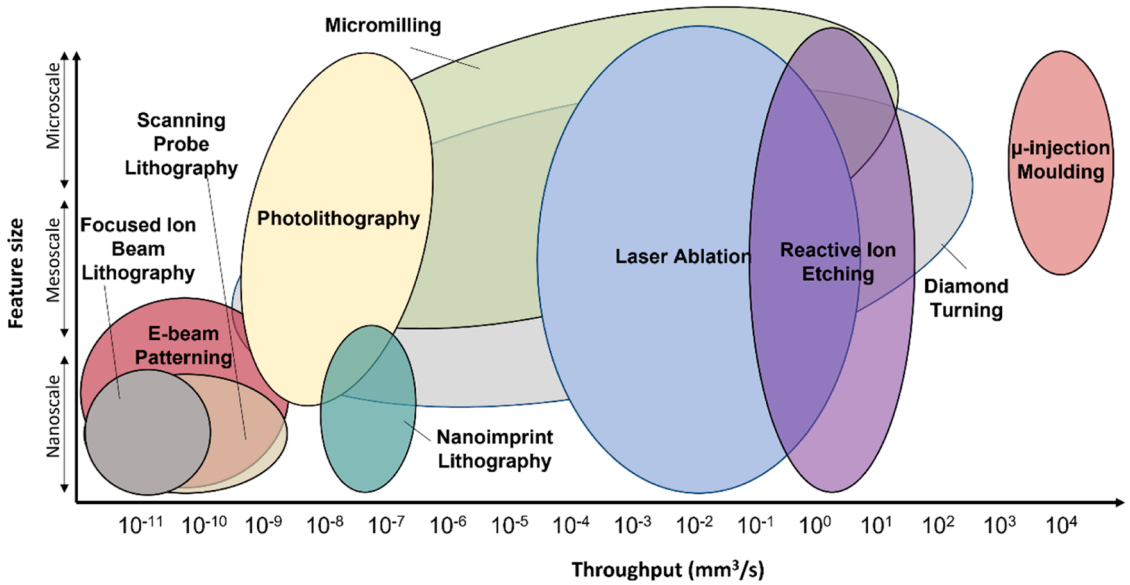

Fig. 2. Ashby style chart showing feature size versus throughput for various micro/nano fabrication methods. This chart is based on general literature, however, highly specialized equipment set-ups could push the magnitudes of feature size and throughput further. Additionally, limitations on studies where the effect of laser wavelength can be directly compared have limited the subsection of laser ablation into femto-, pico- and nanosecond laser ablation. Author's contribution based on the reported literature [15–26].

the structured surfaces can be correlated to its biological function [28].

In pursuit of finding answer to these questions, an experimental campaign was initiated by fabrication and testing of femtosecond laser ablated structured surfaces on stainless steel samples. The fabricated surfaces were extensively characterized to investigate the effect of surface topography (physical properties) and surface energy (physico-chemical properties) on the biological functionality (i.e., ability to inhibit bacterial attachment, whilst maintaining healthy osteoblast attachment) and novel information was derived based on the experimental measurements.

In recent years, fractal dimension analysis has emerged as a powerful tool for quantifying surface topography and its influence on bioactivity, particularly in the context of bacterial and cell adhesion. Reviews by Bacakova et al. [29] and Ferraris et al. [30] have extensively explored the role of surface topography, including fractal analysis, in modulating cell behaviour and bioactivity. The former review focused on biomedical applications, while the latter review highlights the potential of fractal geometry in understanding cell behaviour on biomaterial surfaces. Both reviews concluded that fractal dimension analysis is a robust method for linking surface topography to bioactivity, especially in the context of cell adhesion and proliferation.

Moreover, a review of Anselme et al. [31] highlighted that fractal dimensions, play a critical role in modulating cell and bacterial interactions. They emphasized that surface topography directly influences adhesion mechanisms, making fractal analysis a valuable metric for predicting bioactivity.

Much of the research in this field has been conducted on titanium substrates, where fractal dimension has proven to be a reliable indicator of bioactivity. For instance, Puckett et al. [32] investigated the relationship between titanium surface nanostructure and bacterial adhesion, using fractal dimension as a key parameter. Their results demonstrated that fractal dimensions could quantitatively describe surface features responsible for bacterial attachment, providing a robust framework for predicting bioactivity. Similarly, Mwenifumbo et al. [33] used fractal dimension analysis to study laser-microtextured titanium surfaces and their impact on cell adhesion. Further supporting this, Soboyejo et al. [34] demonstrated that fractal dimension analysis of Ti-6Al-4 V surfaces could predict osteoblast adhesion. They observed that surfaces with specific fractal characteristics enhanced osteoblast attachment, further validating the use of fractal analysis in evaluating bioactivity.

Beyond titanium, studies on other materials, such as borosilicate glass and metallic biomaterials, have also supported the utility of fractal dimension analysis. For example, Preedy et al. [35] investigated the adhesion of *Staphylococcus aureus* to borosilicate glass surfaces with varying fractal dimensions. Their findings revealed that surfaces with intermediate fractal dimensions exhibited optimal bacterial adhesion, underscoring the importance of fractal analysis in understanding bacterial-surface interactions. Additionally, Bigerelle & Anselme [36] used fractal dimension analysis to statistically correlate surface roughness with cell adhesion and proliferation on metallic biomaterials. They found that surfaces with higher fractal dimensions promoted greater cell adhesion, suggesting that fractal analysis is a reliable predictor of cellular response.

2. Manufacturing and materials

2.1. Experimental setup

Rolled stainless steel plates supplied by LASEA Ltd. (Belgium) were cut into 0.5 × 0.5 cm^2. The samples were 0.3 cm thick. The chemical composition of the stainless-steel samples obtained from Energy-dispersive X-ray spectroscopy (EDS) is presented in Table 1.

Laser irradiation was performed using a LASEA LS4 laser machine [37–39] equipped with an amplitude systems satsuma laser source of wavelength 1030 nm and a pulse duration of 400 fs. The laser output was firstly directed through a polarizer and half-wave plate for fine adjustment of the laser pulse energy, before a beam expander to achieve an appropriate beam size (Fig. 3). A galvanometric scanning head (LS scan) and a 100 mm focal length f-theta lens were then employed to

Table 1
Chemical composition of the as-received stainless-steel samples.

Element	Fe	Cr	Mn	C	O	Si
Weight percentage (%)	67.58 ± 1.61	13.44 ± 0.59	9.11 ± 2.52	7.59 ± 2.01	1.66 ± 0.55	0.61 ± 0.50

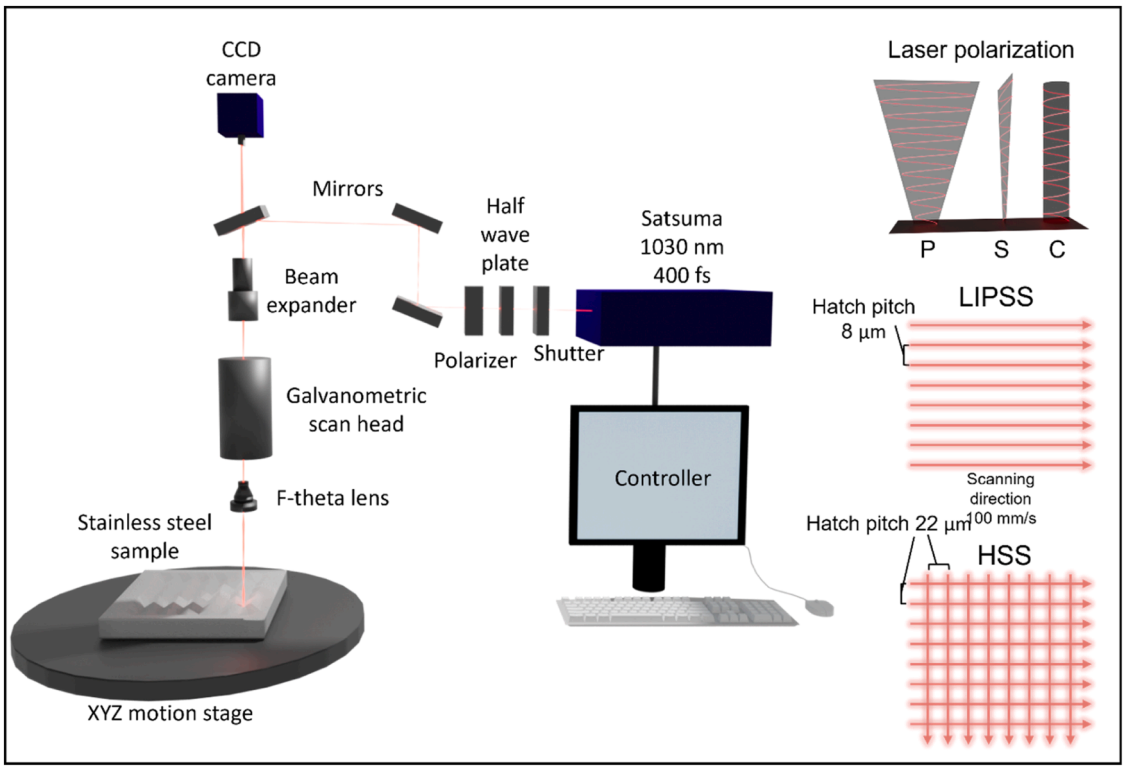

Fig. 3. Laser processing strategy used in this work.

focus the laser beam on the specimen surface. In this work, two types of laser treatments were applied to fabricate (a) nanostructured surfaces and (b) hierarchical micro/nano structured surfaces herein referred to as laser-induced periodic surface structures (LIPSS) and hierarchically structured surfaces (HSS), respectively.

Table 2 lists the processing parameters that were used to generate distinct types of laser-structured surfaces. Herein, the LIPSS surfaces were referred to according to the beam polarization (P, S or C) used to fabricate them namely, LIPSS_P, LIPSS_S and LIPSS_C. Similar to this, the hierarchically structured surfaces were referred to with the number of laser passes applied: HSS_10 and HSS_40. In total, there were 5 different types of samples namely, LIPSS_P, LIPSS_S, LIPSS_C, HSS_10 and HSS_40 which were investigated as part of this study.

Laser fluence (F) varied between the LIPSS and HSS processing but was maintained above the ablation threshold of stainless steel (0.1 J/cm^2) [40] as per the equation:

$$F = \frac{2E_p}{\pi\omega_0^2} \quad (1)$$

where *Ep* is the energy per pulse (0.8 μJ for LIPSS and 5.6 μJ for HSS) and ω_0 is the focal spot size in focus (23 μm).

Table 2
Laser parameters used for fabrication of structured surfaces on stainless steel.

Parameters	LIPSS	HSS
Wavelength (nm), pulse duration (fs)	1030, 400	
Average power (W)	0.1	0.7
Repetition rate (kHz)	125	
Scan speed (mm/s)	100	
Hatch pitch (μm)	8	22
Passes	1	10 or 40
Polarization	P, S, or C	P
Fluence (J/cm^2)	0.385	2.695

2.2. Surface topography assessment

All samples treated by laser were analysed with a Tescan S8215 G field emission (Tescan, Czechia) scanning electron microscope (FE-SEM) at 10 keV and 63 pA to observe the morphological and microstructural changes on the processed surface.

Topography measurements were carried out using a Form Talysurf 120 L surface profilometer (2.5 μm radius and 60° cone angle diamond tip probe) to assess the long wavelength component of the hierarchically structured surfaces, and a (Veeco/DI) Bruker Dimension 3100 with a Nanoscope V controller (Bruker, USA) atomic force microscope (AFM) was used to assess the roughness parameters of all the structured surfaces.

Profiles of 200 μm length were measured using the profilometer for both HSS_10 and HSS_40 surfaces. Three measurements were taken for each sample and the microfeature heights (peak-to-peak) were determined.

The AFM measurements were conducted in tapping mode. The AFM was fitted with a nanoSensors AFM Probe PPP-NCHR-10 tip with a nominal radius of <10 nm and nominal length of 125 μm. The AFM scans were performed for an area of (5 × 5) μm^2. The scan size (5 × 5 μm^2) was chosen to be 512 × 512 to result in a 9.76 nm sampling size commensurate with the tip size used. Three measurements were taken for each sample. Post processing was performed using TalyMap Gold software (7.4, Taylor Hobson Inc., UK). Areal topography parameters such as average areal surface roughness (S_a), root-mean-square roughness (S_q), developed interfacial area ratio (S_{dr}), texture-aspect-ratio (S_{tr}), density of peaks (S_{pd}) and fractal dimension (D) were calculated.

The AFM scans were first levelled line-by-line according to the direction of scanning. S-filter was then applied to denoise the measurement with a cut-off of 0.06 μm [41]. The robust Gaussian filter was then used to assess the surface parameters at varying scales (0.125:0.125:1 μm and 1:1:5 μm).

S_a represents a commonly used parameter to assess the average deviation of the local surface height from the mean plane. It is known,

however, that the average roughness is not sufficient to uniquely describe a surface in relation to the bacterial attachment. S_{dr} is a parameter that describes the percentage of additional surface area contributed by the texture as compared to an ideal plane and can be useful to understand the surface area available for cellular/bacterial contact. The fractal dimension (D) is a measure of complexity of the system which can be determined by various techniques such as the walking-divider method, box/cube-counting method, prism-counting method, Epsilon-Blanket method, perimeter-area relationship and power spectrum method. Among the several techniques which are used to estimate the fractal dimension, the box/cube-counting method is the most popularly used technique for the analysis of two or three-dimensional structures.

2.3. Surface free energy assessment

Deionized water and diiodomethane static contact angles were measured via the sessile drop method with an OCA 25 goniometer (DataPhysics Instruments GmbH, Germany) and the data was analyzed with SCA20 software (DataPhysics Instruments GmbH, Germany). A droplet volume of 2 μL was used for all tests. At least three measurements were taken for each sample after (8–10) s of contact with the sample surface. The results were reported as average value ± standard deviation.

The roughness corrected contact angle (Young's contact angle) was calculated according to the following equations [42]:

$$\cos\theta_m = r\cos\theta_Y \tag{2}$$

$$r = 1 + \frac{S_{dr}}{100} \tag{3}$$

where θ_m is the measured contact angle, θ_Y is Young's contact angle, r is the roughness factor and S_{dr} is the developed interfacial area ratio.

The surface energy (SFE) was then calculated based on the Owens-Wendt-Rabel & Kaelble (OWRK) model [43]:

$$\frac{\gamma_l(\cos\theta_Y + 1)}{2\sqrt{\gamma_l^d}} = \sqrt{\frac{\gamma_s^p\gamma_l^p}{\gamma_l^d}} + \sqrt{\gamma_s^d} \tag{4}$$

where γ_l is the total surface energy of the liquid, γ_l^d and γ_l^p are the dispersive and polar component of the liquid respectively, and γ_s^d and γ_s^p are the dispersive and polar components of the surface. The parameters used to compute the surface energy are shown in Table 3.

It must be noted that the size of the area evaluated through the droplet method is significantly higher than the area evaluated to calculate S_{dr} values. Additionally, since the AFM scans from which S_{dr} values were extracted are 5 × 5 μm^2, not encompassing the full micro-features for the hierarchical laser structured surfaces (HSS surfaces), S_{dr} cannot be used to calculate the corrected contact angle for these surfaces. However, for LIPSS surfaces, given that their dominant wavelength is encompassed within the measurement, S_{dr} values can be used. Therefore, S_{dr} was evaluated at different scales to assess the suitability of its usage to compute the corrected contact angle for these surfaces.

Table 3
Surface energy estimates for distilled water [44] and diiodomethane [45].

Liquid	γ_l(mJ/m^2)	γ_l^p (mJ/m^2)	γ_l^d (mJ/m^2)
Distilled water	72.8	46.8	26
Diiodomethane (≥98 % (GC) from Sigma Aldrich)	50	2.6	47.4

2.4. Chemical analysis

2.4.1. Energy dispersive spectroscopy (EDS)

Energy dispersive spectroscopy analysis was performed on all substrates using an Oxford Instruments Ultim® X-Max 100 mm EDS system (Oxford Instruments, Abingdon, UK) fitted on a Tescan S8215 G (Tescan, Czechia) scanning electron microscopy (SEM) to study the chemical composition of the samples.

2.4.2. X-ray photoelectron spectroscopy (XPS)

X-ray photoelectron spectroscopy (XPS) analysis was performed using a UHV-XPS FlexMod system with a monochromated 400 W Al K anode (SPECS XR-50 M) (SPECS surface nanoanalysis GmbH, Germany). The analyzer used was a Phoibos 150 with 1D delay line detectors.

Measurements were carried out at 10^{-9} mbar. The hydrocarbon component of the C 1 s peak (BE 284.8 eV) was used as a reference for charge correction. Survey spectra were collected in 2 scans with 50 eV pass energy and recorded at 0.5 eV/step and 0.1 s dwell time, while the region spectra were collected in 9 scans with 30 eV pass energy taken at 0.1 eV/ step and 0.1 s dwell time.

The Tougaard algorithm was used to measure the background core level spectra and chemically distinct species in the high-resolution regions of the spectra were resolved using synthetic Gaussian–Lorentzian components and asymmetric line function where applicable (Cr metal and Fe metal) after the background was removed (using CasaXPS software, v. 2.3.25). The relative atomic concentration of elements determined using XPS was quantified based on the peak area in the selected high-resolution region, with the appropriate sensitivity factors for the instrument being used. High-resolution scans were performed across each of chromium 2p (Cr2p) and iron 2p (Fe2p) peaks.

2.5. Bacterial growth

Prior to each bacterial attachment experiment, *S. aureus* NCTC 7791 (Culture Collections, UK Health Security Agency, UK) bacterial cultures were prepared from a single colony on tryptone soya agar (TSA) with pH 7.3 ± 0.2 and grown overnight in tryptone soya broth (TSB) at 37 °C, 5 % CO_2. The overnight bacterial culture (10 ml) was transferred to a universal container and centrifuged at 5000 g for 5 min. The bacterial pellet was then resuspended with PBS and centrifuged again at 5000 g for 5 min. The pellet was resuspended in Phosphate-Buffered Saline (PBS) with pH 7.4 to an optical density (OD600 nm) of 0.09 (corresponding to approximately 1 × 10^7 CFU/ml).

2.6. Bacterial retention study

A 15 μl droplet of the inoculum was added to each sample surface in a 24 -well plate and incubated for 1 hour at 37 °C, 5 % CO_2. The samples were then transferred to a fresh 24-well plate and washed in 1 ml of 0.85 % NaCl. Live/dead staining was performed according to the manufacturer's instructions (LIVE/DEAD BacLight Viability Kit, Thermofisher Scientific, UK) and imaged using an AX-70 fluorescent microscope (Olympus, Japan) at magnifications of x10, x 20 and x40. The percentage area coverage or bacterial coverage (BC) was quantified using ImageJ software as outlined in a previous publication [46] from the x10 magnification images to ensure the largest sample surface area was analysed.

2.7. Osteoblast-like cell culture, attachment and morphology

To assess the biocompatibility/cytotoxicity of the manufactured surfaces, human MG-63 osteoblast-like cells (Sigma Aldrich, UK) were used. Cell attachment was studied to determine favourable surface features for encouraging bone formation while the cell morphology was studied to determine whether surface features may induce cytoskeletal changes and therefore influence osteogenic potential. Cells (passages

29–32) were seeded at 5000 cells/cm^2 and maintained in T75 cell culture flasks in culture medium comprising of alpha minimum essential medium (α-MEM) supplemented with 10 % (v/v) heat-inactivated foetal bovine serum (FBS) and 100 units/ml penicillin G sodium (Assay: 96.0–102.0 %), 0.1 μg/ml streptomycin sulphate and 0.25 μg/ml amphotericin (Thermofisher Scientific, UK). The cells were incubated at 37 °C, 5 % CO_2 and the medium were changed every 2–3 days. Cells were cultured until they reached approximately 80–90 % confluency before being used for subsequent experiments.

The cells were detached using trypsin-EDTA 0.25 %, counted and seeded directly on the control surfaces and the laser structured surfaces in a 24-well plate at a density of 100 cells/μl (approximately 1500 cells per sample). Samples were incubated for 1 h at 37 °C, 5 % CO_2 to allow attachment. The wells were then flooded with 500 μl of complete culture media and incubated for a further 24 h.

Subsequently, the samples were washed three times with PBS (pH 7.4) to remove non-adherent cells and incubated in 500 μl of 10 % formalin overnight at 4 °C to fix the attached cells. Following incubation, the formalin solution was removed, and the samples were washed three times with tris-buffered saline (TBS). The cells were then permeabilized with filtered 1 % high purity Triton X-100 (Sigma Aldrich, UK) for 30 min at room temperature. After permeabilization, the samples were washed three times with TBS. Incubation of the samples for 1 hour at room temperature with a solution of 1 % bovine serum albumin (Vector Laboratories, UK) in TBS was performed to block non-specific binding sites. Following incubation, the actin filaments of the cells were stained with freshly prepared fluorescein isothiocyanate (FITC) labelled phalloidin (diluted 1:50 in TBS, Sigma Aldrich, UK) and incubated in the dark for 40 mins at room temperature. The samples were then washed three times with TBS and allowed to air dry for 5 min. Subsequently,10 μl of 4′,6-diamidino-2-phenylindole (Assay > 98 % from DAPI, Vector Laboratories, UK) was added to each sample surface to stain the nuclei of the cells. Images of the cell actin filaments and nuclei were taken at magnifications of x10, x20, x40 using an AX70 Olympus fluorescent microscope (Olympus, Japan). FITC and DAPI channels were superimposed using ImageJ. Cell attachment and morphology analysis was performed on the fluorescent images to semi-quantify the area of the cells (CA), the circularity of the cells (CC) and the cell number (CN), where applicable using ImageJ image processing software.

2.8. Statistical analysis

Contact angle measurements, AFM measurements and cell culture experiments were performed three times for all surfaces. Bacterial attachment experiments were performed twice, and three images (x10) were taken at random and analyzed for each sample. The Shapiro wilk test was conducted on all results to validate the normal distribution for all experiments. All data were subject to a one-way analysis of variance (ANOVA) to test for statistical significance. A p-value of ≤ 0.05 was considered significant whereas in the case of a p-value of > 0.05, the results were reported as observational. In the case that the ANOVA-obtained p-value was found to be <0.05, Tukey's multiple comparisons test was performed to obtain pairwise comparisons between data means. All data were expressed as the mean accompanied by the standard deviation.

To determine the correlation between bacterial attachment, surface energy and topographical roughness parameters, as well as the correlation between surface energy, topographical roughness parameters and MG-63 cell-related parameters. Correlation matrices were constructed using the Spearman correlation factor. The MG-63 cell-related parameters included the number of attached cells (CN), cell area (CA) and cell circularity (CC).

3. Results

3.1. Characterisation of laser-fabricated micro/nano patterned surfaces

Fig. 4(a) shows the electron microscopy examination of the laser-fabricated nanometric structures processed at low fluence values. In Fig. 4(a), various nanometric features such as ridges, ripples, and peaks with various spatial frequencies can be seen. It is evident from Fig. 4(a) that surfaces subjected to low fluence laser irradiation undergo reorganization, resulting in the formation of a distinct surface morphology which is commonly referred to as "laser-induced periodic surface structures" (LIPSS).

LIPSS_P and LIPSS_S surfaces were both exposed to a linearly polarized laser beam whereas LIPSS_C was exposed to a circularly polarized laser beam. The direction of the incident electrical laser field is indicated with red arrows, a circle and the scanning direction is indicated with the white arrow. LIPSS_P and LIPSS_S presented a similar pattern of parallel nano-ridges linked together by short nano-ripples as depicted in Fig. 4(b).

Nanospheres can also be observed on LIPSS_P and LIPSS_S. The structure of LIPSS_C was a nano-ripple dominated structure with a few visible circular nano-peaks. In some instances, nanoripples can be seen clustered together longitudinally (top right of LIPSS_C 10kx SEM micrograph in Fig. 4(a)).

The dimensions of nanoripples present on the LIPSS surfaces were estimated from SEM image analysis which are shown in Fig. 4(c).

The AFM height maps of different surfaces are shown in Fig. 5(a), along with the dominant surface wavelength obtained through the power spectrum density method. The structured surfaces showed a significantly lower dominant wavelength than the flat surface. It is crucial to consider this aspect for understanding the relevance of feature wavelength (scale) in relation to bacteria-surface and MG-63-surface interactions which is discussed later.

The roughness parameters, on varying scales (0.125:0.125:1 μm and 1:1:5 μm) were extracted from filtered AFM height maps. In particular, the roughness parameters at the 0.5 μm scale are shown in Fig. 5(b). Fig. 5(b) presents results for roughness measurements and the fractal dimension of HSS surfaces.

On all scales, including 0.5 μm, LIPSS_P possesses higher S_a than LIPSS_S which corroborates with the nano-ridges height measurement. The developed interfacial area ratio increases from a flat surface to a structured surface. The highest S_{dr} was in the case of LIPSS_P for all scales. The peak density parameter was lowest for LIPSS_P, followed by the flat surface, then LIPSS_S and highest for LIPSS_C. The fractal dimension, describing the surface complexity was highest for LIPSS_C as shown in Fig. 5(c,d).

Surfaces that have been exposed to high fluence laser revealed a hierarchical structure that consists of regularly spaced micron-sized bumps superimposed with nanoridges, nanopeaks and nanoripples as presented in the SEM micrographs in Fig. 6(a). A few deep micro-holes can be seen on the surface exposed to 40 laser passes (HSS_40).

The topography of the HSS surfaces presents two features, which can be viewed in short and long range wavelengths, the short one is amenable to AFM measurements whilst the long one is amenable to profilometry measurements as shown in Fig. 6(b). The long wavelength component contains microfeatures while the short wavelength contains nanofeatures sitting on top of the microfeatures. Together they are referred to as hierarchical structures.

Profilometry line scans depicting the primary profile of the hierarchical surfaces are presented in Fig. 6(c). The height of the microfeatures of HSS_10 was lower than that of HSS_40, as expected, due to the increased number of laser passes.

S_{dr} values were plotted against all evaluated scales for LIPSS surfaces (Fig. 7). All the structured surfaces exhibited significantly lower SFEs compared to the flat surface. Within LIPSS surfaces, LIPSS_P exhibited the lowest SFE of 23.4 mJ/m^2. Within HSS surfaces, the surface energy

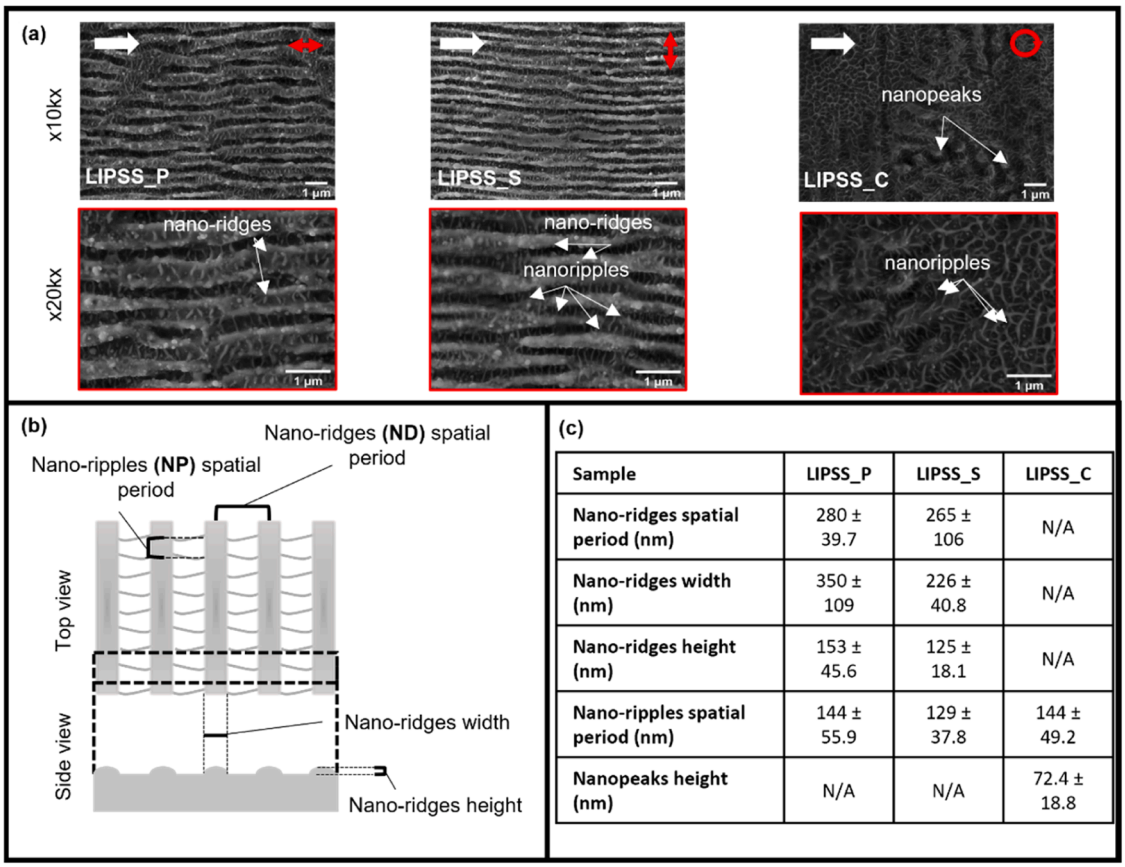

Sample	LIPSS_P	LIPSS_S	LIPSS_C
Nano-ridges spatial period (nm)	280 ± 39.7	265 ± 106	N/A
Nano-ridges width (nm)	350 ± 109	226 ± 40.8	N/A
Nano-ridges height (nm)	153 ± 45.6	125 ± 18.1	N/A
Nano-ripples spatial period (nm)	144 ± 55.9	129 ± 37.8	144 ± 49.2
Nanopeaks height (nm)	N/A	N/A	72.4 ± 18.8

Fig. 4. (a) SEM micrographs of the three types of SS surfaces. The red arrows indicate the laser polarization and the white arrows indicate the scanning direction. (b) Diagram depicting the typical linearly polarized LIPSS morphology. (c) Geometrical measurements of nanoripples and nano-ridges of LIPSS surfaces measured from SEM image processing. The heights were measured from line scans extracted from AFM measurements.

was lowest for the HSS_40 surface, while it was comparable to LIPSS_P for HSS_10.

EDS analysis was performed on all tested samples which is presented in Fig. 8(a). The measurement of different elements did not show significant changes between the samples except for the case of iron and carbon where there was a significant decrease between the flat sample and LIPSS_C for iron, and LIPSS_C and HSS_10 for both iron and carbon.

To better understand the chemical nature of the surface modification, X-ray photoelectron spectroscopy (XPS) measurements were conducted. The XPS binding energy values (in eV) of C 1 s, Cr 2p, Fe 2p, and O 1 s for different samples (LIPSS_P and HSS_10) and the flat sample are presented in Fig. 8(b) and Table 4. It was observed that the carbon content in all samples was significant due to surface contamination. However, the laser structured samples showed approximately 30 % more carbon content than the non-structured samples. As the laser-textured samples had a larger surface area, they had more exposure to carbon-based compounds in the air, resulting in a greater amount of carbon contamination.

This difference in carbon content is also evident in the survey spectra, where a larger carbon peak can be observed for the laser-structured sample. The high-resolution spectra of the chromium and iron peaks confirmed the presence of an oxide layer on all three types of samples. Fig. 8(c) shows the high-resolution spectra of Cr 2p peaks and their deconvolutions. The spectra were fitted with four major components; Cr metal, Cr_2O_3, $Cr(OH)_3$ and $FeCr_2O_4$ according to data found in the literature [47]. The high-resolution Fe 2p spectra are shown in Fig. 8 (d). The peak was fitted with six components belonging to Fe metal, FeO, Fe^{2+} and Fe^{3+} of Fe_3O_4, Fe_2O_3 and FeF_3, according to the data found in the literature regarding peak positions, peak line shapes and widths of individual components [48]. The deconvolution allowed the identification of the different oxidation states of iron and chromium present on the sample's surface and the quantification of their relative amounts as presented in Table 5 and Table 6. The results revealed traces of Cr metal on laser-structured surfaces, while Fe metal was barely present on the surfaces and the surfaces were composed mostly of Cr_2O_3, $Cr(OH)$, $FeCr_2O_4$, and Fe^{3+} with small amounts of Fe^{2+}, Fe_2O_3, FeO and FeF_3. Further explanation of these results is offered in the discussion section.

3.2. Evaluation of bacterial coverage

Fluorescent imaging results following the live/dead assay on the tested surfaces are presented in Fig. 9(a). The coverage or attachment of bacteria shown in Fig. 9(a, b) decreased for all the structured surfaces compared to the flat control surface. The results clearly showed that the highest number of attached bacteria was on the flat unstructured surface with a bacteria coverage percentage of around 4.91 %, followed by LIPSS_P (2.87 %), LIPSS_S (2.53 %) with the lowest attachment for LIPSS type surfaces being on the LIPSS_C surface with 1.80 % bacterial coverage. The HSS surfaces exhibited even lower bacterial coverage with 1.59 % for HSS_10 and 0.53 % for HSS_40. A high negative correlation was mainly observed on the lower scales (0.125 – 0.5 µm) for both S_{tr} and D with the bacterial coverage as shown in Fig. 9(c). The correlation of BC and D was only statistically significant ($p \leq 0.05$) at the 0.375 µm and 0.5 µm scales. Fig. 9(d) depicts the variation of bacteria coverage with the fractal dimension at the 0.5 µm analysis scale.

3.3. Assessment of osteoblast attachment and cell morphology

Following seeding and 24 h of incubation of MG-63 cells on the

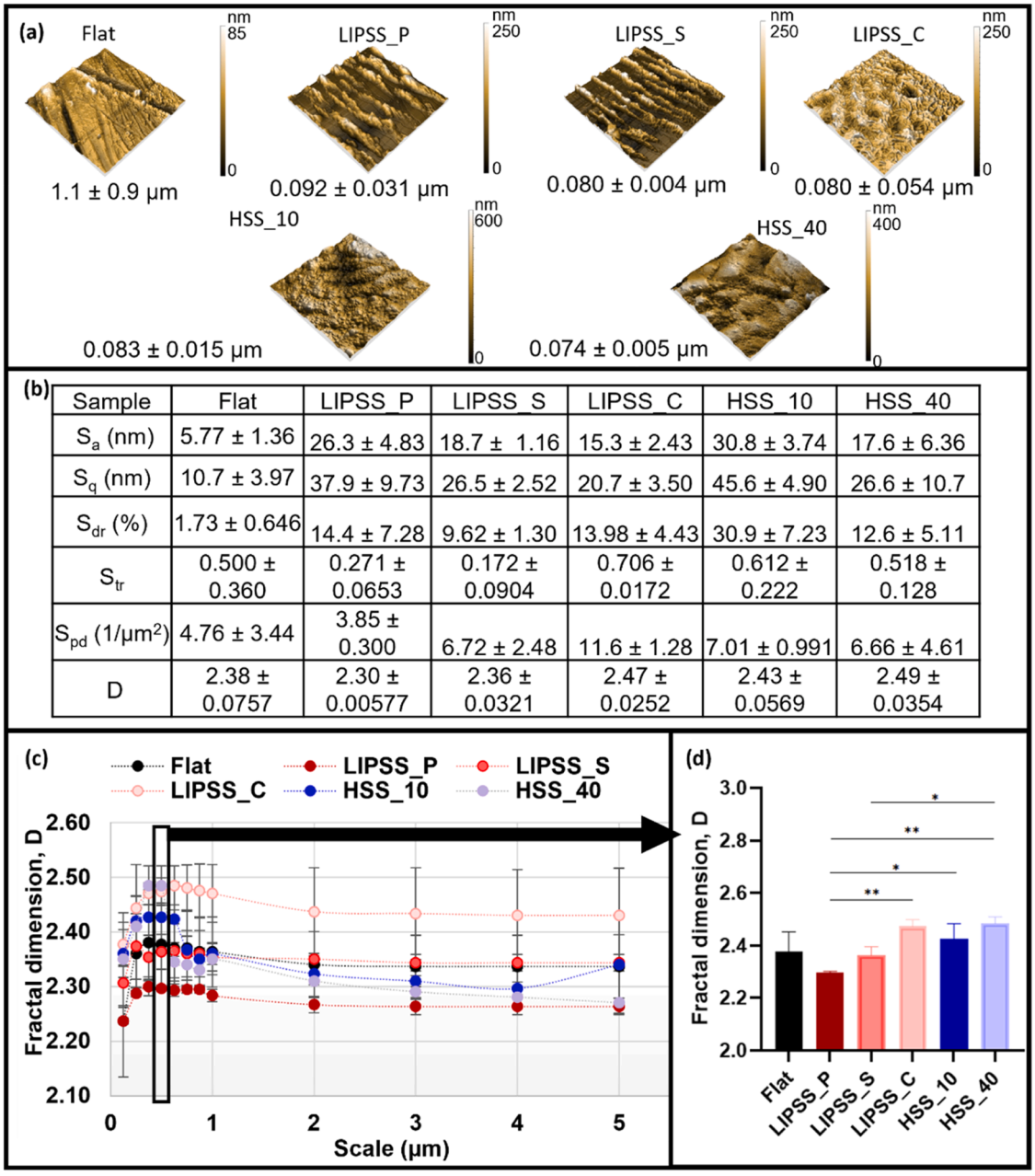

(b) Sample	Flat	LIPSS_P	LIPSS_S	LIPSS_C	HSS_10	HSS_40
S_a (nm)	5.77 ± 1.36	26.3 ± 4.83	18.7 ± 1.16	15.3 ± 2.43	30.8 ± 3.74	17.6 ± 6.36
S_q (nm)	10.7 ± 3.97	37.9 ± 9.73	26.5 ± 2.52	20.7 ± 3.50	45.6 ± 4.90	26.6 ± 10.7
S_{dr} (%)	1.73 ± 0.646	14.4 ± 7.28	9.62 ± 1.30	13.98 ± 4.43	30.9 ± 7.23	12.6 ± 5.11
S_{tr}	0.500 ± 0.360	0.271 ± 0.0653	0.172 ± 0.0904	0.706 ± 0.0172	0.612 ± 0.222	0.518 ± 0.128
S_{pd} (1/µm^2)	4.76 ± 3.44	3.85 ± 0.300	6.72 ± 2.48	11.6 ± 1.28	7.01 ± 0.991	6.66 ± 4.61
D	2.38 ± 0.0757	2.30 ± 0.00577	2.36 ± 0.0321	2.47 ± 0.0252	2.43 ± 0.0569	2.49 ± 0.0354

Fig. 5. (a) AFM height maps of all tested surfaces indicating the corresponding surface's wavelength based on the power spectrum density calculations. (b) Surface topographical parameters of the surfaces at the 0.5 µm scale (c) The fractal dimension of the samples at varying scales. (d) The fractal dimension of the sample at the 0.5 µm scale. The p-value for pairwise comparison between samples and the flat sample are represented by * ($p \leq 0.05$) and ** ($p \leq 0.005$).

structured surfaces, the attachment was observed using fluorescent microscopy which is shown in Fig. 10(a). The cell area (CA), cell number (CN) and cell circularity (CC) were evaluated for all surfaces. The cell area analysis showed a significant difference between most surfaces presented in Fig. 10(b). The average cell area on the flat surface was highest while surface HSS_40 exhibited the lowest significant reduction in cell area. The number of cells attached, although not significantly different among the samples, was highest on the flat surface and lowest on HSS_40. The number of cells attached on HSS_10 was around double the number of cells attached on HSS_40. The cell circularity analysis did not show significant differences however, the circularity of MG-63 cells on HSS_40 was the highest.

A plot depicting the absolute values of the correlation parameters between surface topographical parameters and the MG-63 cell area is presented in Fig. 10(c). A high positive correlation between CA, S_{pd} was found at very low (< 0.25 µm) and high scales (> 4 µm).

Additionally, at scales above 0.625 µm, the CA highly correlated with the fractal dimension. The S_{pd} correlated well on all analysis scales with CN and D highly correlated with CN above 0.625 µm. Finally, the CC correlated strongly with D for low scales (< 3 µm) with statistical significance at very low scales (< 0.5 µm). S_a, S_q, S_{pd} correlated well with CC within the range of scales 0.375 – 0.875 µm. Additionally, Str correlates highly with CC on all scales.

4. Discussions

4.1. Surface treatment, topographical properties and surface chemistry

As anticipated, the LIPSS ridges orientation very much depends on the laser polarization [49]. Since both polarizations P and S were linear,

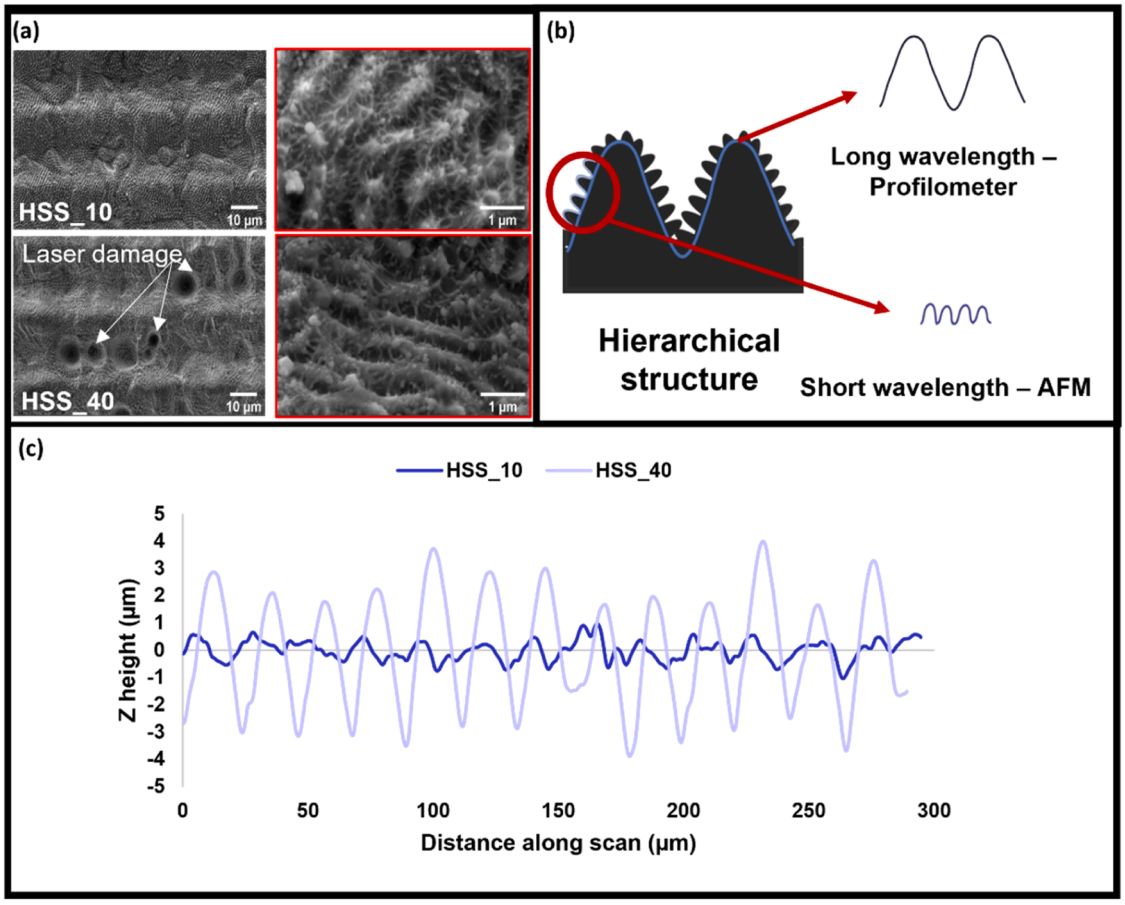

Fig. 6. (a) SEM micrographs of HSS surfaces. (b) Diagram depicting the dual scale topography of HSS surfaces (c) Profilometry line scan of HSS surfaces.

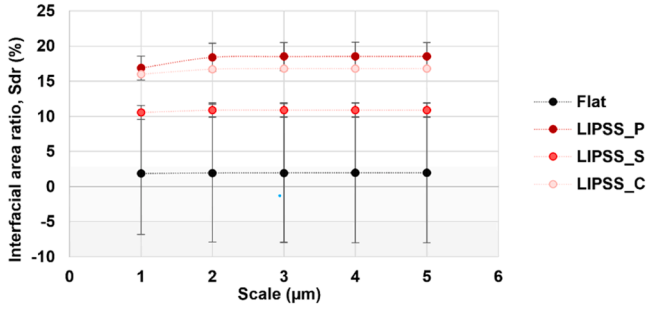

Fig. 7. Surface interfacial area ratio S_{dr} values for Flat and LIPSS surfaces over varying scales.

the resulting surface morphology after irradiation was similar. However, for the case of LIPSS_C, the morphology was observed to be slightly different, as nanoripples were distributed irregularly in some areas and showed some alignment patterns in other areas. The surface complexity of LIPSS_C was corroborated by the high fractal dimension D at all evaluation scales. The LIPSS structure period for all the LIPSS surfaces was $<0.14\lambda$ (λ is the laser wavelength, 1030 nm) which indicated that the surfaces could be classed as high-spatial-frequency LIPSS (HSFL) [49]. The nanospheres observed on the LIPSS_P and LIPSS_S surfaces were due to the redeposition during ablation [50].

The increase in the laser passes from 10 to 40 for HSS surfaces led to an expected increase in the microfeature height, a decrease in the width and an increased slope. The increase in microfeature height was proportional to the number of laser passes. The deep micro-holes observed on HSS_40 resemble single-shot crater ablation. Their morphology reflects the energy distribution within the laser beam, which in this case appears to have a distorted Gaussian distribution [51].

Laser structuring can influence the surface chemistry of alloyed materials such as stainless steel due to the preferential ablation of some alloy components and oxidation reactions on the surface layer. Although the XPS spectra showed that there was generally no significant effect of structuring on the presence of chromium and iron compounds, the main observed difference in the chemical composition of the surface layer was in the fractions of chromium and iron oxides formed on the surface. Particularly, there was a slight increase in the fraction of $Cr(OH)_3$, $FeCr_2O_4$ and Fe^{2+} of Fe_3O_4 for the laser-structured surfaces. However, the difference in the fraction of $Cr(OH)_3$ and Fe^{2+} of Fe_3O_4 between the structured surface was very small. The presence of fluoride was similar in all samples. Considering that fluoride was not detected through EDS but only through XPS, high-resolution scans as FeF_3, the fluoride is most probably present on the outermost surface and/or in very low concentrations (<0.1 wt %) [52]. According to the XPS results, laser irradiation did not significantly affect the fraction of FeF_3. The flat and laser-structured surfaces were both found to be covered with carbon contamination from the environment. Carbon possesses adsorptive qualities which enrich organic nutrients. This can serve as a bioactive component, which can promote early-stage osseointegration and potentially improve biocompatibility, yet it can also encourage bacterial attachment [53]. However, these results do not suggest that the surface chemistry of the samples processed by different laser treatments differed significantly.

4.2. *Influence of surface chemistry on surface biological functionality*

The X-ray photoelectron spectroscopy results indicated that the

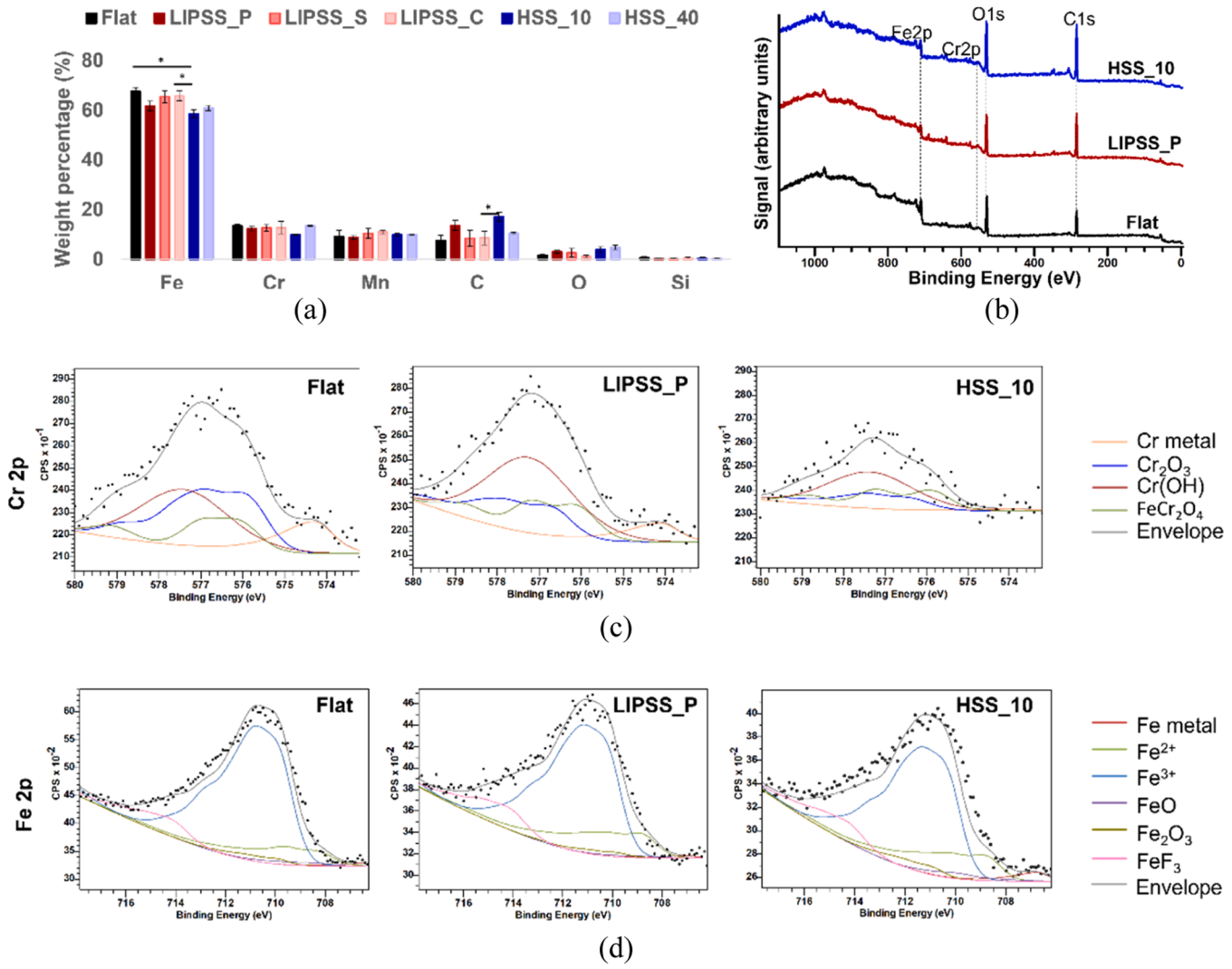

Fig. 8. (a) Chemical composition of the samples obtained from EDS. (b) XPS spectra of representative samples; flat, LIPSS_P and HSS_10 (c) fraction of chromium compounds and (d) fraction of iron compounds.

Table 4
XPS binding energy values (in eV) of C 1 s, Cr 2p, Fe 2p, and O 1 s for different samples, corresponding to Fig 8(b).

Sample	C 1s	Cr 2p	Fe 2p	O 1s
Flat	51.15	1.64	11.2	36.01
LIPSS_P	65	0.73	3.76	30.51
HSS_10	64.42	1.86	4.43	29.29

Table 5
Fraction of chromium compounds corresponding to Fig 8(c).

Cr 2p	Cr metal	Cr_2O_3	CrOH	$FeCr_2O_4$
Flat	13.13	37.2	32.84	16.83
LIPSS_P	8.47	21.61	47.26	22.66
HSS_10	2.15	20.6	47.99	29.26

structured surfaces exhibit a modest difference in chemical composition compared to the flat surface. The percentage of elemental chromium was lower, while the percentage of chromium oxides was higher on the structured surfaces. Trivalent chromium, which was found on all the test surfaces, is known for its high stability and low toxicity as it is understood to be unable to penetrate biological cell membranes [54].

Table 6
Fraction of iron compounds corresponding to Fig 8(d).

Fe 2p	Fe metal	Fe_3O_4 (Fe^{2+})	Fe_3O_4 (Fe^{3+})	Fe_2O_3	FeO	FeF_3
Flat	0.81	11.59	75.76	2.42	1.51	7.91
LIPSS_P	0.46	16.55	70.58	1.8	0.66	9.95
HSS_10	2.73	16.57	66.55	3.3	2.28	8.57

Nevertheless, the change in the fractions of chromium oxides between the structured surfaces did not appear to reflect the biological functionalities observed. At first glance, the detection of FeF_3 may raise concerns, but upon further examination, it was apparent that the fraction of FeF_3 was almost consistent across all samples tested and did not exhibit any discernible correlation with biological functionality.

Thus, the results suggest that surface chemistry is not the primary factor contributing to the reduced bacterial attachment and the changes in the morphology and attachment of MG-63 cells on the surfaces structured by laser in this investigation.

4.3. *Influence of surface topographical properties on surface energy*

It is well-established that surface topography has a considerable influence on surface wettability. More particularly, two distinct wetting

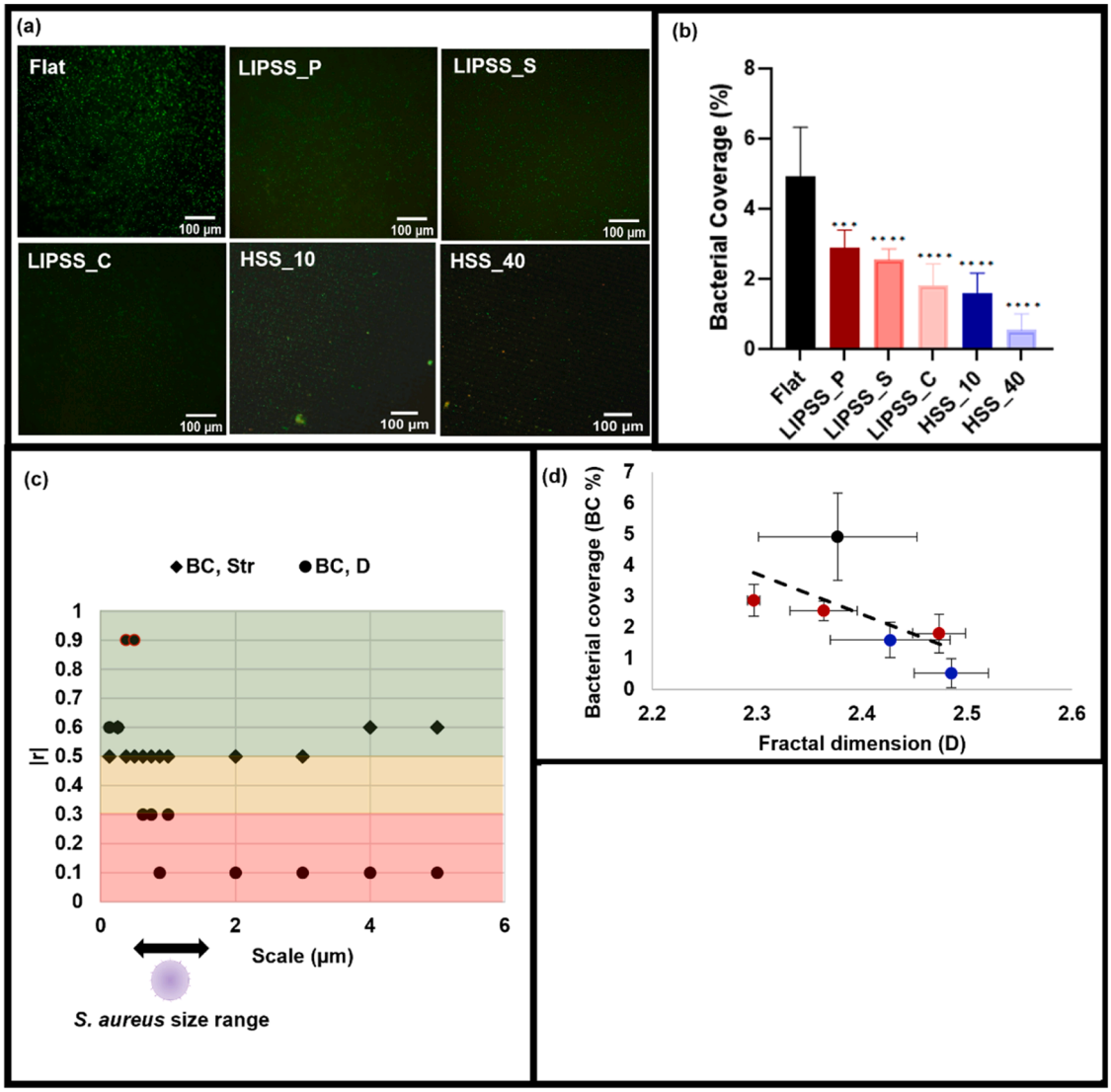

Fig. 9. (a) Fluorescent images of *S. aureus* bacteria attached to the tested surfaces. (b) The bacterial coverage on the tested surfaces. The p-value for pairwise comparison between samples and the flat sample is represented by *** ($p \leq 0.0005$) and **** ($p \leq 0.0001$). (c) The absolute value of correlation factors between the bacterial coverage, the texture aspect ratio and the fractal dimension across scales. Red region: no correlation. Yellow region: weak correlation. Green region: strong correlation. (d) The variation of bacterial coverage with the fractal dimension at 0.5 µm analysis scale.

behaviours for liquid droplets on a rough surface have been defined in the literature: the Wenzel and the Cassie-Baxter state. The Wenzel state proposes that the droplet fills the surface and its micro/nanofeatures, whereas the Cassie-Baxter model proposes that the droplet cannot fill the surface asperities; instead, air is entrapped between the gaps of the surface features. The contact angle can then be expressed using the following equation:

$$\cos\theta_{CB} = f_1 \cos\theta_Y - f_2 \tag{5}$$

The wetting behaviour of the droplet on a nanostructured surface will depend on whether or not the droplet can overcome the energy barrier and wet the micro-nanofeature gaps. This depends on the topography of the surface, its amplitude and spatial characteristics. Those characteristics can be described by roughness parameters, mainly amplitude and spatial parameters. The results indicated that, on the roughness scale, with the increase of amplitude parameters such as S_a and S_q and the hybrid parameter S_{dr}, the surface energy decreases, for both types of surfaces.

The results show that, for HSS-type surfaces, the surface energy (SFE) was lower than for LIPSS surfaces with similar roughness and hybrid parameters. For example, when comparing HSS_10 and LIPSS_C, both of which have similar S_a values, the SFE of HSS_10 was lower than that of LIPSS_C. Similarly, when comparing HSS_40 and LIPSS_C with similar S_{dr}, the SFE of HSS_40 was significantly lower. This difference in SFE can be attributed to the presence of microfeatures on these surfaces. In the case of HSS surfaces, the SFE decreases with the small width and high slope of the microfeature. These variations in the slope and width directly affect the fraction of the solid surface in contact with the droplet, reducing its value. As a result, the contact angle increases, leading to a decrease in the surface energy for HSS surfaces compared to LIPSS surfaces, as predicted by Eq. (5).

4.4. Influence of surface energy on bacterial adhesion

The surface energy of a surface has been established to have an influence on bacterial adhesion as established by the XDLVO theory and further reinforced by experimental data [55,56]. Furthermore, surface energy affects the bacteria-containing liquid by influencing how it wets the surface. If a surface possesses a low SFE, the liquid droplet does not spread, thus the interfacial solid/liquid area available for bacteria to

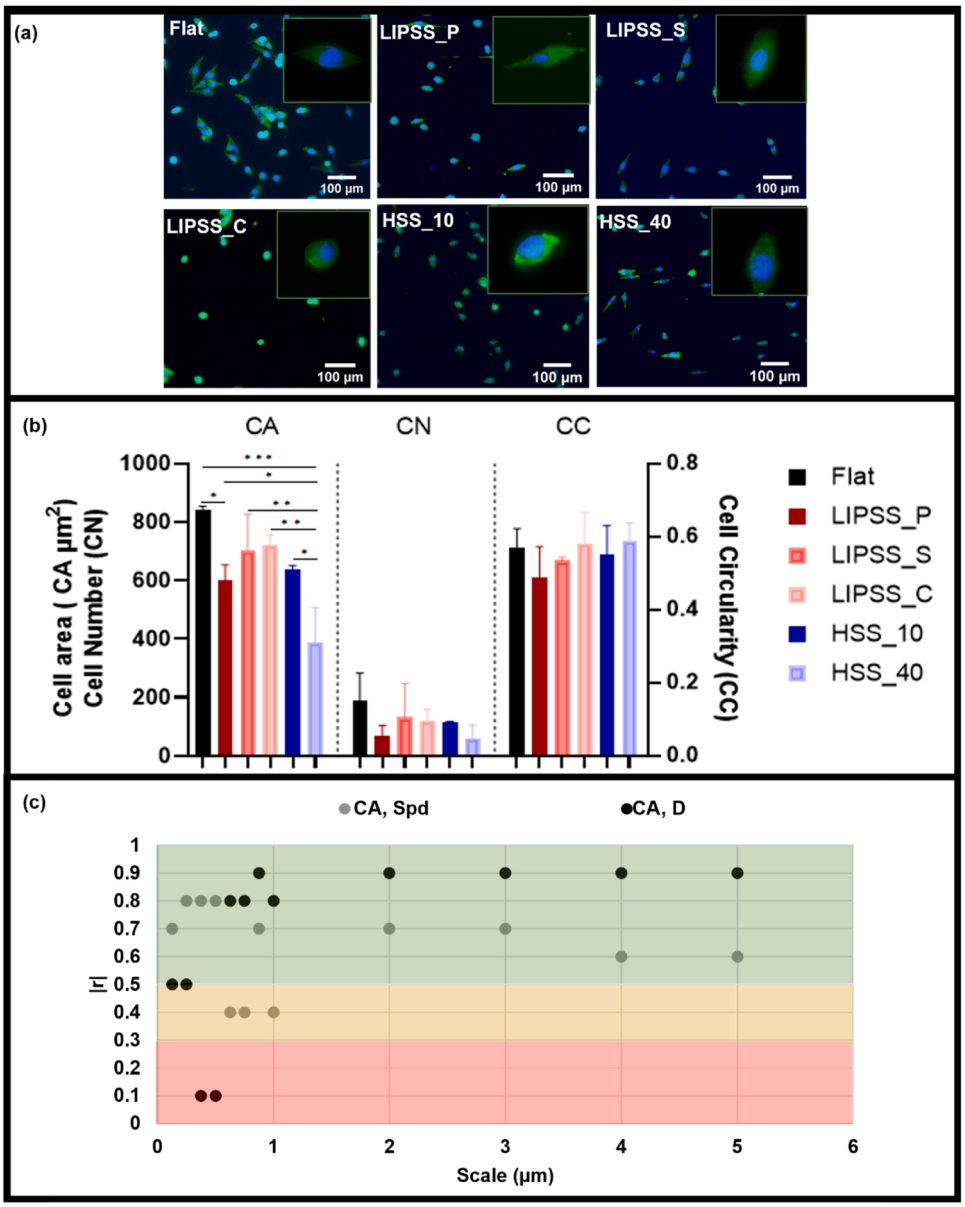

Fig. 10. (a) Fluorescent microscopy images of MG-63 cells attached to the tested surfaces. (b) The Cell area (CA), cell number (CN) and cell circularity (CC) of the MG-63 cells attached to the tested surfaces. (c) The absolute value of the correlation factors for the cell area, density of peaks and the fractal dimension across scales. In this case, both correlations are positive.

adhere is less than that for a high SFE surface as depicted in Fig. 11(a).

When bacteria are near the surface, the surface energy (i.e. the sum of the van der Waals attraction, the electrostatic repulsion and the acid-base interaction) also affects their adhesion to the surface as described by the XDLVO theory [57]. For instance, when comparing two smooth surfaces with varied surface energies, Liu and Zhao (2005) [58] observed that the increase in the surface energy scales linearly with the bacterial attachment. There are contradictions in the literature concerning this and an opposite trend has also been reported [59]. Additionally, when surface structuring is introduced, this interaction becomes more complex as structuring is known to influence not only surface energy but also surface area available for bacteria to attach. Surface structuring, relative to the studied bacterium size, might expose a larger area for attachment increasing the probability of bacterial adhesion. Alternatively, it may make an exposed area physically unreachable to the bacterium. In this study, it was observed that surfaces with low surface energies (in the range of 19.5–32 mJ/m^2) exhibited a decrease in bacterial attachment compared to the high SFE flat surface as seen in Fig. 9. However, when comparing structured surfaces together, no correlation between the surface energy and the bacterial coverage was found ($r_{SFE,BC} = 0.30$), indicating that surface energy is not the primary factor in the reduction of bacterial attachment on structured surfaces.

4.5. *Influence of surface topography on bacterial adhesion*

The *S. aureus* retention study showed a clear decrease in bacterial coverage on all the structured surfaces compared to the unstructured flat surface. The reduction of bacterial attachment relative to the flat surface was approximately 41 % for LIPSS_P, 48 % for LIPSS_S and 63 % for LIPSS_C. While the reduction was 67 % for HSS_10 and 89 % for HSS_40 surfaces compared to the flat surface.

The dominating wavelength of the structured surfaces correlated strongly (positively) with bacterial coverage ($r_{wavelength,BC} = 0.67$). Considering that the wavelength of the surfaces ranged between 0.074 and 1 µm, this correlation indicated that the bacterial attachment

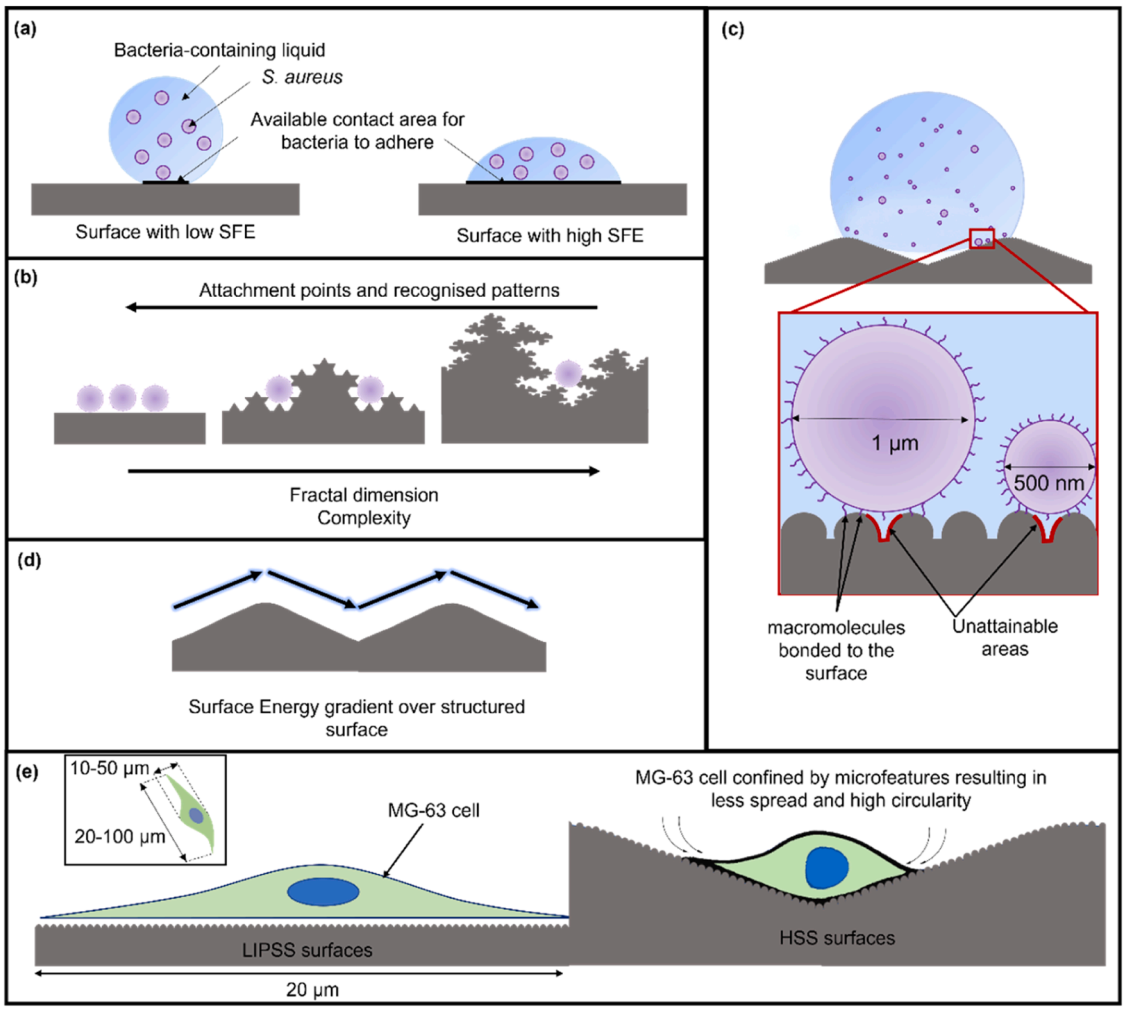

Fig. 11. Cartoon illustration showing (a) the initial effect of surface energy on available solid/liquid contact area for bacteria to attach. (b) The effect of a high fractal dimension or surface complexity on bacterial adhesion. (c) Surface nano-structuring hinders bacterial macromolecule attachment due to the creation of unattainable areas. (d) Surface energy gradient on hierarchically structured surfaces. (e) MG-63 cell spread is hindered by microfeature spacing. The inset is showcasing the typical size range for MG-63 cells (Not to scale).

increases when the wavelength of the features increases to values comparable or beyond the bacterium size.

There still exists a divide in the literature as to whether roughness correlates positively or negatively with bacterial adhesion. That is mainly due to an oversimplification of the surface topography assessments and lack of comprehensive surface roughness analysis leading to the masking of underlying surface patterns or features.

The results of this study do not show any correlation between S_a, S_q on any scale and the bacterial coverage (BC). The parameter S_{tr} correlates (negatively) very well with the bacterial coverage at scales lower than 1 µm. This means that when S_{tr} of a structured surface is high, BC is low. In other words, anisotropic surface features encourage bacterial attachment while isotropy discourages it. The lack of directional cues on high S_{tr} surface topographies makes it more difficult for the adhesion complexes and proteins to find and bind to their specific binding sites on the surface, reducing the overall adhesion strength, and ultimately reducing adhesion [60]. In this study, the fractal dimension was uniquely employed for the first time as an attempt to establish a scalar indicator for complex surfaces, to advance the understanding on this front. The results of the fractal dimension analysis over various scales are presented in Fig. 5(c).

The analysis (Fig. 9) revealed a strong negative correlation between the fractal dimension (D) and bacterial adhesion at scales below 0.5 µm.

A surface with a high degree of complexity (high D) can decrease adhesion sites for bacteria, as depicted in Fig. 11(b), making it more difficult for them to establish a foothold on the surface. This in turn disrupts bacterial attachment as is evident in the results. Particularly for *S. aureus*, it has been observed that when they attach to surfaces with low SFE, they use multiple macromolecules that bind weakly to the surface, such as serine-aspartate repeat-containing protein C [25]. On the other hand, when they attach to high SFE surfaces, they use fewer macromolecules that bind more strongly.

Therefore, for the bacteria to attach to the LIPSS and HSS surfaces, which are surfaces with low SFE, it is likely that *S. aureus* requires attachment of a large number of macromolecules/macromolecule patches of sizes ranging between (0.1 to 0.5) µm [61,62], which can be hindered by the complexity of the surface structure on that scale as illustrated in Fig. 11(b, c). Furthermore, if the macromolecules were to bind to the complex surface, the molecules would impart stresses on the bacterium's membrane forcing it to deform, which creates an inopportune situation for bacterial adhesion [63]. These results suggest that bacteria do not favour complexity and isotropy for attachment. The results also suggest that the fractal dimension, evaluated at scales comparable to the bacterium and its macromolecule sizes, can be a stronger indicator of bacterial response to specific surface topographies than the surface energy ($r_{D,BC}$ at low scales > $r_{SFE,BC}$).

Hierarchically structured surfaces have been observed to possess better antibacterial properties than LIPSS surfaces, and this may be due

to the ability of hierarchical structuring to induce localized surface energy gradients as illustrated in Fig. 11(d) [64]. This means that the surface may not be stable for a particular microorganism with a specific surface energy requirement to attach, suggesting that the hierarchical structuring has the potential to prevent bacterial attachment and colonization. However, it should be noted that these are observations and require further research to confirm their validity. Material residual stresses, though not explored in this study, could also be contributing to the decrease in adhesion on structured surfaces. For instance, Bagherifard et al. [65] have shown that enhanced surface compressive residual stresses in the material surface decrease bacterial attachment on shot-peened stainless steel surfaces. Concurrently, some studies have shown that laser processing increases compressive residual stresses [66].

4.6. Correlation of surface parameters with MG-63 cell adhesion

The adherence of MG-63 cells to biomaterials is a multifaceted phenomenon influenced by various factors, ranging across various scales. The examination of the interaction between MG-63 cells and patterned surfaces indicated that the expansion of MG-63 cells, notably the cell area, is substantially impacted by the surface energy, the fractal dimension and the density of peaks. Since the change in surface area was the only cell-bound parameter that changed with statistical significance, all other parameters discussed concerning the cells' morphologies (CN and CC) are considered observational only. The decrease in SFE between the flat and structured surfaces is highly correlated with a decrease in cell area ($p_{Flat/LIPSS\_P} 1 < 0.05$ & $p_{Flat/HSS\_40w} < 0.0001$). This finding is in agreement with the literature where high SFE was found to induce spatial osteoblastic cell growth and enhance the area of cells compared to low SFE surfaces [67]. Although the decrease in surface energy between the flat and structured surfaces corresponded to a decrease in MG-63 osteoblast attachment (CN), it is noteworthy that this decrease was not observed to be statistically significant.

The current results, shown in Fig. 10(c), suggest that at very low scales (< 0.375 μm) there is a weak positive correlation between the surface complexity and the cell area. However, at scales higher than 0.5 μm, the correlation becomes strong, indicating that MG-63 cell spread increases with increasing degrees of surface complexity. Similar results have been presented in the literature where it was shown that random and disordered nanoscale topography enhanced osteo-specific differentiation of human mesenchymal cells [68]. In addition, a positive correlation was found between the number of cells on the surface and the fractal dimension on scales greater than 0.5 μm. However, increasing surface complexity hurts cell circularity. In particular, it was found that the fractal dimension has a positive correlation with cell circularity on scales smaller than 1 μm, with a significant correlation on scales smaller than 0.5 μm. This suggests that MG-63 cells tend to attach preferentially to surfaces with high fractal dimensions, but their morphology is not favourable on these types of surfaces.

The peak density of small wavelength features (< 0.25 μm) positively correlates with CA, the correlation drops for features with wavelengths between 0.5 μm and 0.875 μm, then increases with wavelengths features (> 1 μm).

Extracellular matrix (ECM) molecules such as fibronectin, vitronectin, laminin and collagen, mediate cell attachment to surfaces and vary widely in size. For instance, collagen fibrils have diameters ranging from 0.05 to 0.3 μm and can also assemble to make larger cable-like collagen fibers that could reach a size of 4 μm in diameter [69]. The hierarchy in surface adhesins explains the correlations found at varying scales, owing that MG-63 cells are affected to dissimilar degrees by different wavelength features due to the specific interaction of varying size macromolecules with the surface features. Not only that but adhesins and ECM components can grow differently depending on the surface topography. For instance, a study reported that on patterned surfaces (<0.5 feature sizes) MG-63 cells exhibited larger stress fibers and thinner actin filaments compared to flat surfaces [69]. More research is required to understand the preferential attachment of different adhesins to differently sized surface features, and how the surface patterning affects the growth of MG-63 cell ECM components.

Besides these parameters, microfeatures also affect the spread of MG-63 cells, particularly when the spatial frequency of the microfeatures is similar to the typical size of the cells (diameter: 20–50 μm, length: 20–100 μm) [70,71]. This hindered the cell spreading process as illustrated in Fig. 11(e), indicating that the presence of microfeatures plays a crucial role in regulating the behaviour of MG-63 cells by controlling their ability to spread and their subsequent morphology.

Generally, nanostructures (LIPSS) did not significantly affect the attachment and morphology of MG-63 cells regardless of the difference in topographical and surface energy parameters (except for LIPSS_P, $p = 0.0205$). However, the presence of microfeatures, particularly deep microfeatures (HSS_40) significantly reduced the cell area and observably decreased the number of cells attached.

4.7. Limitations of this research

Like many studies, this work has certain limitations, primarily arising from restricted access to instruments and the number of repeat trials conducted. The study is divided into three main sections: (1) laser fabrication, (2) surface characterisation, and (3) bioassays. The limitations associated with each of these sections are discussed below.

4.7.1. Limitations with the fabrication strategy

The laser-fabricated steel samples were produced in a single batch using fixed parameters derived from the literature [37–39] and approved by the industrial partner LASEA. This restricts the ability to evaluate the reproducibility of the fabrication process under varying conditions, such as fluctuations in laser power, environmental factors, or material inconsistencies. This alludes to the reliance on predefined industrial and literature-based parameters that may not be optimised for different compositions. Investigating a broader range of parameters could reveal a different metallurgical structure on the micromachined laser surface. It is also worth noting that all samples used in this research were produced from a single batch of stainless steel, meaning any inherent variability in material properties (e.g., composition, surface roughness) could influence the results. Its composition obtained from the instrument was highlighted earlier in Table 1 but steel samples with composition that are used to fabricate real medical implants could be incorporated into this test procedure for more improved evaluation. Repeating the fabrication process with different material batches would help confirm the repeatability and generalizability of the findings.

4.7.2. Limitations with surface characterisation strategy

Due to limited access to the instrument, XPS measurements were performed only once which limits the reproducibility of the surface chemistry analysis. Repeating XPS measurements at multiple locations would help verify the consistency of the surface composition and identify potential anomalies or contamination. As opposed to this while the AFM and contact angle measurements were repeated three times, the sample size may still be insufficient to fully capture variability in surface topography and wettability. Increasing the number of replicates or testing additional samples could provide more robust statistically reliable conclusions.

4.7.3. Limitations with bioassay test results

Despite performing cell culture experiments three times, biological systems inherently exhibit variability due to factors such as cell passage number, culture conditions and operator technique. This variability could affect the reproducibility of the bioassay results. Also, while technical replicates (e.g., triplicate wells) were included, the study may have been constrained by the number of biological replicates (e.g., independent cell cultures). Increasing the number of biological replicates would enhance the statistical power and generalizability of the findings.

It can also be pointed out that the bioassays were conducted within a specific timeframe, which may not account for potential time-dependent effects, such as long-term cell behaviour or changes in surface properties over time. Extending the duration of the experiments or conducting time-point analyses could reveal new time-dependent details in the analysis.

5. Conclusions

This study explored the impact of femtosecond laser ablation on the bioactivity of stainless-steel surfaces, focusing on the adhesion and attachment of *Staphylococcus aureus* NCTC 7791 and MG-63 osteoblast-like cells. Surfaces produced via femtosecond laser ablation, characterized by dominant wavelengths smaller than the size of the bacteria and comparable to the dimensions of surface-adhering macromolecules, exhibited reduced adhesion and attachment of *S. aureus* NCTC 7791. Additionally, these hierarchical structured surfaces influenced the attachment and morphology of MG-63 cells, highlighting their dual functionality in antibacterial activity and cell response.

To address the fundamental question of whether surface roughness affects bacterial adhesion, we conducted a comprehensive evaluation of various surface roughness parameters. Our findings reveal that commonly used parameters, such as mean average roughness (Ra) and peak-to-valley roughness (Rt), are inadequate for describing cell adhesion and surface bioactivity. Instead, we propose the "fractal dimension" as a more effective metric for characterizing surfaces in this context.

Our analysis demonstrates a clear correlation between fractal dimension and bioactivity, highlighting its impact on the adhesion of *Staphylococcus aureus* NCTC 7791 and MG-63 osteoblast-like cells. Specifically, fractal dimension and peak density significantly influenced MG-63 cell attachment and morphology, particularly cell area. Notably, the presence of deep microfeatures inhibited cell spreading.

Importantly, laser-induced periodic structured surfaces (LIPSS) with sub-micron wavelengths, high fractal dimension, and high texture aspect ratio emerged as promising candidates for regulating surface bioactivity. These surfaces achieved a 63 % reduction in bacterial colonization compared to flat surfaces while maintaining cytocompatibility with MG-63 cells.

These results underscore the potential of laser-induced structured surfaces for advancing antibacterial strategies and promoting osseointegration, paving the way for further exploration and optimization.

Data statement

Data supporting this study are included in the article

CRediT authorship contribution statement

Sara Hawi: Writing – original draft, Software. **Saurav Goel:** Writing – review & editing, Supervision, Funding acquisition, Data curation. **Vinod Kumar:** Writing – original draft, Resources. **Claudiu Giusca:** Writing – review & editing. **Oliver Pearce:** Writing – review & editing. **Wayne Nishio Ayre:** Writing – original draft, Resources, Project administration.

Declaration of competing interest

The authors declare that they have no known competing financial interests or personal relationships that could have appeared to influence the work reported in this paper.

Acknowledgments

All authors acknowledge the financial support provided by the UKRI via Grant No EP/T024607/1. We are particularly grateful to LASEA ltd. for assisting us with sample fabrication using their facilities based in Belgium, Cambridge Royce facilities grant EP/P024947/1 and Sir Henry Royce Institute - recurrent grant EP/R00661X/1.

Data availability

Data will be made available on request.

References

[1] S. Zhang, C.L. Wong, S. Zeng, R. Bi, K. Tai, K. Dholakia, M. Olivo, Metasurfaces for biomedical applications: imaging and sensing from a nanophotonics perspective, Nanophotonics 10 (2021) 259–293.
[2] L. Xu, M. Rahmani, Programmable structured surfaces can change the future of wireless communications, Light 11 (2022) 196.
[3] A. Jaggessar, H. Shahali, A. Mathew, P.K.D.V. Yarlagadda, Bio-mimicking nano and micro-structured surface fabrication for antibacterial properties in medical implants, J. Nanobiotechnol. 15 (2017) 64.
[4] T. Özel, D. Biermann, T. Enomoto, P. Mativenga, Structured and textured cutting tool surfaces for machining applications, CIRP Annals 70 (2021) 495–518.
[5] X. Jiang, P.J. Scott, D.J. Whitehouse, L. Blunt, Paradigm shifts in surface metrology. Part II. The current shift, in: Proceedings of the Royal Society A: Mathematical, Physical and Engineering Sciences 463, 2007, pp. 2071–2099.
[6] S. Arango-Santander, Bioinspired topographic surface modification of biomaterials, Materials 15 (2022) 2383.
[7] K.P. Sheahan, G. Bowens, A. MacLellan, P. Kenny, E.O. Neill, Prospective surveillance of post-operative surgical site infection in orthopedic patients undergoing hip procedures-lessons learnt over A seven-year surveillance program, Biomed. J. Sci. Tech. Res. 49 (2023) 40782–40787.
[8] R. Coello, A. Charlett, J. Wilson, V. Ward, A. Pearson, P. Borriello, Adverse impact of surgical site infections in english hospitals, J. Hospital Infect. 60 (2005) 93–103.
[9] M. Larrañaga-Altuna, A. Zabala, I. Llavori, O. Pearce, D.T. Nguyen, J. Caro, H. Mescheder, J.L. Endrino, G. Goel, W.N. Ayre, Bactericidal surfaces: an emerging 21st-century ultra-precision manufacturing and materials puzzle, Appl. Phys. Rev. 8 (2021).
[10] N.K. Katiyar, G. Goel, S. Hawi, S. Goel, Nature-inspired materials: emerging trends and prospects, NPG. Asia Mater. 13 (2021) 56.
[11] M. Zhang, S. Feng, L. Wang, Y. Zheng, Lotus effect in wetting and self-cleaning, Biotribology 5 (2016) 31–43.
[12] L. Feng, S. Li, Y. Li, H. Li, L. Zhang, J. Zhai, Y. Song, B. Liu, L. Jiang, D. Zhu, Superhydrophobic surfaces: from natural to artificial, Adv. Mater. 14 (2002) 1857–1860.
[13] D.P. Linklater, V.A. Baulin, S. Juodkazis, R.J. Crawford, P. Stoodley, E.P. Ivanova, Mechano-bactericidal actions of nanostructured surfaces, Nature Rev. Microbiol. 19 (2021) 8–22.
[14] A. Malshe, K. Rajurkar, A. Samant, H.N. Hansen, S. Bapat, W. Jiang, Bio-inspired functional surfaces for advanced applications, CIRP Annals 62 (2013) 607–628.
[15] J.-M. Romano, M. Gulcur, A. Garcia-Giron, E. Martinez-Solanas, B.R. Whiteside, S. S. Dimov, Mechanical durability of hydrophobic surfaces fabricated by injection moulding of laser-induced textures, Appl. Surf. Sci. 476 (2019) 850–860.
[16] A. Grigorescu, C. Hagen, Resists for sub-20-nm electron beam lithography with a focus on HSQ: state of the art, Nanotechnology 20 (2009) 292001.
[17] R. Garcia, A.W. Knoll, E. Riedo, Advanced scanning probe lithography, Nat. Nanotechnol. 9 (2014) 577–587.
[18] C. Fanara, P. Shore, J.R. Nicholls, N. Lyford, J. Kelley, J. Carr, P. Sommer, A new reactive atom plasma technology (RAPT) for precision machining: the etching of ULE® surfaces, Adv. Eng. Mater. 8 (2006) 933–939.
[19] M.I. Mgwatu, Integrated approach for optimising machining parameters, tool wear and surface quality in multi-pass turning operations, Adv. Product. Eng. Manage. 8 (2013).
[20] A. Schubert, S. Groß, B. Schulz, U. Eckert, Sequential combination of micro-milling and laser structuring for manufacturing of complex micro-fluidic structures, Phys. Procedia 12 (2011) 221–229.
[21] S.N. Bhavsar, S. Aravindan, P.V. Rao, Investigating Material Removal Rate and Surface Roughness Using Multi-Objective Optimization For Focused Ion Beam (FIB) Micro-Milling of Cemented Carbide, 40, Precision Engineering, 2015, pp. 131–138.
[22] P. Pou-Álvarez, A. Riveiro, X. Nóvoa, M. Fernández-Arias, J. Del Val, R. Comesaña, M. Boutinguiza, F. Lusquiños, J. Pou, Nanosecond, picosecond and femtosecond laser surface treatment of magnesium alloy: role of pulse length, Surf. Coat. Technol. 427 (2021) 127802.
[23] S.N. Bhavsar, S. Aravindan, P.V. Rao, Machinability study of high speed steel for focused ion beam (FIB) milling process–An experimental investigation at micron/nano scale, Precis. Eng. 38 (2014) 168–173.
[24] K.E. Hix, M. Li, J. Gosciniak, K. Hartke, M. Rendina, L.R. Dosser, M. Alexander, Femtosecond and nanosecond laser micromachining of oxidized multi-wall carbon nanotube doped morthane. Photon Processing in Microelectronics and Photonics IV, SPIE, 2005, pp. 157–168.
[25] U. Loeschner, J. Schille, A. Streek, T. Knebel, L. Hartwig, R. Hillmann, C. Endisch, High-rate laser microprocessing using a polygon scanner system, J. Laser Appl. 27 (2015).
[26] M. Altissimo, E-beam lithography for micro-/nanofabrication, Biomicrofluidics. 4 (2010).

[27] H. Qin, H. Cao, Y. Zhao, G. Jin, M. Cheng, J. Wang, Y. Jiang, Z. An, X. Zhang, X. Liu, Antimicrobial and osteogenic properties of silver-ion-implanted stainless steel, ACS Appl. Mater. Interfaces 7 (2015) 10785–10794.
[28] M. Larrañaga-Altuna, A. Zabala, I. Llavori, O. Pearce, D.T. Nguyen, J. Caro, H. Mescheder, J.L. Endrino, G. Goel, W.N. Ayre, R.K. Seenivasagam, D.K. Tripathy, J. Armstrong, S. Goel, Bactericidal surfaces: an emerging 21st-century ultra-precision manufacturing and materials puzzle, Appl. Phys. Rev. 8 (2021) 021303.
[29] L. Bacakova, E. Filova, M. Parizek, T. Ruml, V. Svorcik, Modulation of cell adhesion, proliferation and differentiation on materials designed for body implants, Biotechnol. Adv. 29 (2011) 739–767.
[30] S. Ferraris, S. Spriano, Antibacterial titanium surfaces for medical implants, Mater. Sci. Eng. C 61 (2016) 965–978.
[31] K. Anselme, P. Davidson, A. Popa, M. Giazzon, M. Liley, L. Ploux, The interaction of cells and bacteria with surfaces structured at the nanometre scale, Acta Biomater. 6 (2010) 3824–3846.
[32] S.D. Puckett, E. Taylor, T. Raimondo, T.J. Webster, The relationship between the nanostructure of titanium surfaces and bacterial attachment, Biomaterials 31 (2010) 706–713.
[33] S. Mwenifumbo, M. Li, J. Chen, A. Beye, W. Soboyejo, Cell/surface interactions on laser micro-textured titanium-coated silicon surfaces, J. Mater. Sci. 18 (2007) 9–23.
[34] W.O. Soboyejo, C. Mercer, S. Allameh, B. Nemetski, N. Marcantonio, J.L. Ricci, Multi-scale microstructural characterization of micro-textured Ti-6Al-4V surfaces, Key. Eng. Mater. (2001).
[35] E. Preedy, S. Perni, D. Nipič, K. Bohinc, P. Prokopovich, Surface roughness mediated adhesion forces between borosilicate glass and gram-positive bacteria, Langmuir 30 (2014) 9466–9476.
[36] M. Bigerelle, K. Anselme, Statistical correlation between cell adhesion and proliferation on biocompatible metallic materials, J. Biomed. Mater. Res. Part A 72 (2005) 36–46.
[37] V.M. Villapún, K. Man, L. Carter, P. Penchev, S. Dimov, S. Cox, Laser texturing of additively manufactured implants: a tool to programme biological response, Biomater. Adv. 153 (2023) 213574.
[38] L. González-Fernández, A. Anagnostopoulos, T. Karkantonis, S. Dimov, M. Chorążewski, Y. Ding, Y. Grosu, Laser-texturing of stainless steel as a corrosion mitigation strategy for high-temperature molten salts applications under dynamic conditions, Solar Energy Mater. Solar Cells 257 (2023) 112380.
[39] T. Karkantonis, A. Gaddam, X. Tao, T.L. See, S. Dimov, The influence of processing environment on laser-induced periodic surface structures generated with green nanosecond laser, Surf. Interfaces 31 (2022) 102096.
[40] A. Peter, A.H.A. Lutey, S. Faas, L. Romoli, V. Onuseit, T. Graf, Direct laser interference patterning of stainless steel by ultrashort pulses for antibacterial surfaces, Opt. Laser Technol. 123 (2020) 105954.
[41] N. Senin, Feature-based characterisation of areal surface topography. Characterisation of Areal Surface Texture, Springer, 2024, pp. 181–244.
[42] R.N. Wenzel, Resistance of solid surfaces to wetting by water, Indus. Eng. Chem. 28 (1936) 988–994.
[43] D.K. Owens, R.C. Wendt, Estimation of the surface free energy of polymers, J. Appl. Polym. Sci. 13 (1969) 1741–1747.
[44] H.J. Busscher, A.W.J. van Pelt, P. de Boer, H.P. de Jong, J. Arends, The effect of surface roughening of polymers on measured contact angles of liquids, Colloids Surf. 9 (1984) 319–331.
[45] R.N. Shimizu, N.R. Demarquette, Evaluation of surface energy of solid polymers using different models, J. Appl. Polym. Sci. 76 (2000) 1831–1845.
[46] W.N. Ayre, T. Scott, K. Hallam, A.W. Blom, S. Denyer, H.K. Bone, J.P. Mansell, Fluorophosphonate-functionalised titanium via a pre-adsorbed alkane phosphonic acid: a novel dual action surface finish for bone regenerative applications, J. Mater. Sci. 27 (2016) 1–12.
[47] M. Biesinger, C. Brown, J. Mycroft, R. Davidson, N. McIntyre, X-ray photoelectron spectroscopy studies of chromium compounds, Surf. Interface Anal. 36 (2004) 1550–1563.
[48] A. Grosvenor, B. Kobe, M.C. Biesinger, N. McIntyre, Investigation of multiplet splitting of Fe 2p XPS spectra and bonding in iron compounds, Surf. Interface Anal. 36 (2004) 1564–1574.
[49] O. Varlamova, J. Reif, S. Varlamov, M. Bestehorn, The laser polarization as control parameter in the formation of laser-induced periodic surface structures: comparison of numerical and experimental results, Appl. Surf. Sci. 257 (2011) 5465–5469.
[50] S. Shin, J.K. Park, D.-H. Kim, Suppression of spallation induced nanoparticles by high repetition rate femtosecond laser pulses: realization of precise laser material processing with high throughput, Opt. Express. 29 (2021) 20545–20557.
[51] M. Shaheen, J. Gagnon, B. Fryer, Laser ablation of iron: a comparison between femtosecond and picosecond laser pulses, J. Appl. Phys. (2013) 114.
[52] A.S.H. Makhlouf, M. Aliofkhazraei, Handbook of Materials Failure Analysis With Case Studies from the Oil and Gas Industry, Butterworth-Heinemann, 2015.
[53] M. Hočevar, B.Š. Batič, M. Godec, V. Kononenko, D. Drobne, P. Gregorčič, The interaction between the osteosarcoma cell and stainless steel surface, modified by high-fluence, nanosecond laser pulses, Surf. Coat. Technol. 394 (2020) 125878.
[54] D. McGregor, R. Baan, C. Partensky, J. Rice, J. Wilbourn, Evaluation of the carcinogenic risks to humans associated with surgical implants and other foreign bodies—A report of an IARC Monographs Programme Meeting, Eur. J. Cancer 36 (2000) 307–313.
[55] Y. Yuan, M.P. Hays, P.R. Hardwidge, J. Kim, Surface Characteristics Influencing Bacterial Adhesion to Polymeric Substrates, 7, RSC advances, 2017, pp. 14254–14261.
[56] M. Hermansson, The DLVO theory in microbial adhesion, Colloids Surf. B 14 (1999) 105–119.
[57] Y. Cheng, G. Feng, C.I. Moraru, Micro- and nanotopography sensitive bacterial attachment mechanisms: a review, Front. Microbiol. 10 (2019).
[58] Y. Liu, Q. Zhao, Influence of surface energy of modified surfaces on bacterial adhesion, Biophys. Chem. 117 (2005) 39–45.
[59] J.K. Oh, Y. Yegin, F. Yang, M. Zhang, J. Li, S. Huang, S.V. Verkhoturov, E. A. Schweikert, K. Perez-Lewis, E.A. Scholar, T.M. Taylor, A. Castillo, L. Cisneros-Zevallos, Y. Min, M. Akbulut, The influence of surface chemistry on the kinetics and thermodynamics of bacterial adhesion, Sci. Rep. 8 (2018) 17247.
[60] J.J.T.M. Swartjes, D.H. Veeregowda, Implications for directionality of nanoscale forces in bacterial attachment, Biophys. Rep. 1 (2015) 120–126.
[61] H. Khateb, R.S. Sørensen, K. Cramer, A.S. Eklund, J. Kjems, R.L. Meyer, R. Jungmann, D.S. Sutherland, The role of nanoscale distribution of fibronectin in the adhesion of Staphylococcus aureus studied by protein patterning and DNA-PAINT, ACS. Nano 16 (2022) 10392–10403.
[62] S.P. Nair, R.J. Williams, B. Henderson, Advances in our understanding of the bone and joint pathology caused by Staphylococcus aureus infection, Rheumatology 39 (2000) 821–834.
[63] M.I. Ishak, J. Jenkins, S. Kulkarni, T.F. Keller, W.H. Briscoe, A.H. Nobbs, B. Su, Insights into complex nanopillar-bacteria interactions: roles of nanotopography and bacterial surface proteins, J. Colloid. Interface Sci. 604 (2021) 91–103.
[64] S. Zhang, J. Huang, Z. Chen, Y. Lai, Bioinspired special wettability surfaces: from fundamental research to water harvesting applications, Small. 13 (2017) 1602992.
[65] S. Bagherifard, D.J. Hickey, A.C. de Luca, V.N. Malheiro, A.E. Markaki, M. Guagliano, T.J. Webster, The influence of nanostructured features on bacterial adhesion and bone cell functions on severely shot peened 316L stainless steel, Biomaterials 73 (2015) 185–197.
[66] D. Kumar, G. Liedl, A. Otto, W. Artner, Insights into the correlation between residual stresses, phase transformation, and wettability of femtosecond laser-irradiated ductile iron, Nanomaterials 12 (2022) 1271.
[67] J.Y. Lim, M.C. Shaughnessy, Z. Zhou, H. Noh, E.A. Vogler, H.J. Donahue, Surface energy effects on osteoblast spatial growth and mineralization, Biomaterials 29 (2008) 1776–1784.
[68] M.J. Dalby, N. Gadegaard, R. Tare, A. Andar, M.O. Riehle, P. Herzyk, C.D. W. Wilkinson, R.O.C. Oreffo, The control of human mesenchymal cell differentiation using nanoscale symmetry and disorder, Nat. Mater. 6 (2007) 997–1003.
[69] W.-B. Tsai, Y.-C. Ting, J.-Y. Yang, J.-Y. Lai, H.-L. Liu, Fibronectin modulates the morphology of osteoblast-like cells (MG-63) on nano-grooved substrates, J. Mater. Sci. 20 (2009) 1367–1378.
[70] J.B. Nebe, L. Müller, F. Lüthen, A. Ewald, C. Bergemann, E. Conforto, F.A. Müller, Osteoblast response to biomimetically altered titanium surfaces, Acta Biomater. 4 (2008) 1985–1995.
[71] J.-Y. Yang, Y.-C. Ting, J.-Y. Lai, H.-L. Liu, H.-W. Fang, W.-B. Tsai, Quantitative analysis of osteoblast-like cells (MG63) morphology on nanogrooved substrata with various groove and ridge dimensions, J. Biomed. Mater. Res. Part A 90A (2009) 629–640.